Lasers, Balls & Nanomotors

Force-Dependent Substrate Translocation in FtsH: A Single-Molecule Optical Tweezers Study of a Thermophilic AAA+ Protease

Maarten Slik

Delft University of Technology

TU Delft

Lasers, Balls & Nanomotors

Force-Dependent Substrate Translocation in FtsH: A Single-Molecule Optical Tweezers Study of a Thermophilic AAA+ Protease

by

Maarten Slik

to obtain the degree of Master of Science,
at the Delft University of Technology,
and the Erasmus University of Rotterdam,
to be defended publicly on Tuesday December 16, 2025 at 13:00.

Student number:	4883430	
Project duration:	March, 2025 – December, 2025	
Thesis committee:	P. Y. Wang,	Supervisor
	Dr. M. E. Aubin-Tam,	First examiner
	Dr. K. S. Grußmayer,	Second examiner
	Dr. M. Depken,	Third examiner

Cover: Battle between Titin-boi and FtsH drawn by Maarten Slik

TU Delft

Abstract

FtsH is a universally conserved, membrane-bound AAA+ protease critical for the quality control of membrane proteins. While the nanomechanics of homologous proteases have been widely studied, the nanomechanical profile of FtsH, remains largely unexplored. This thesis investigates the hyperthermophilic FtsH variant from *Aquifex aeolicus* using single trap optical tweezers.

First, we validated the functional integrity of detergent-solubilized AaFtsH through bulk biochemical assays. We demonstrated robust proteolytic activity against both disordered (β-casein) and structured (titin-I27 variants) at the experimental optical trapping temperature of 50°C.

To distinguish sub-nanometer motor steps from the high thermal fluctuations and instrumental drift inherent to high-temperature experiments, we conducted a rigorous system noise analysis and validation. We demonstrated that standard step-finding algorithms can be optimized through a novel Allan Variance-based Kalafut-Visscher step-fitting (AVKV) method and released it as an open-source Python toolkit. This workflow objectively determines optimal resampling bandwidth, ensuring that step detection is driven by statistical rigor.

Using this validated AVKV framework, we resolved distinct translocation events by FtsH characterized by a mean step size of 1.15 ± 0.64 nm and a step dwell time of 0.29 ± 0.28 s. Notably, repeated unfolding patterns were not observed for the titin-V13P substrate, likely due to a combination of mutation and elevated temperature rendering the substrate unstable.

Collectively, this work provides the first single-molecule observation of processive stepping by AaFtsH and establishes a standardized, reproducible computational framework for analyzing optical tweezers data in high-noise environments.

Contents

List of Figures

List of Tables

Nomenclature

If a nomenclature is required, a simple template can be found below for convenience. Feel free to use, adapt or completely remove.

Abbreviations

Abbreviation	Definition
AAA+	ATPases Associated with diverse cellular Activities
AaFtsH	Aquifex aeolicus FtsH
AV	Allan variance
BSA	Bovine Serum Albumine
DHFR	dihydrofolate reductase
FtsH	Filamentous temperature-sensitive H
GWN	Gaussian white noise
ITO	Indium Tin Oxide
OT	Optical tweezers
PSD	Position sensing detector
SA	Streptavidin
ssrA	Small stable RNA A

Symbols

Symbol	Definition	Unit
Da	Molecular weight	[kg]
f	frequency	[Hz]
F	Force	[N]
k	Trap stiffness	[pN/nm]
g	Gravitational constant	
M	Molar concentration	[mol L^{-1}]
OD_λ	Optical density at a specific wavelength	[au]
Pa	Pressure	[$N \cdot m^{-2}$]
P	Power	[W]
λ	Wavelength	[nm]
Δr	Bead to trap distance	[nm]
ρ	Density	[kg/m^3]
σ_τ^2	Allan variance	nm^2
τ	Sampling period	s

1

General Introduction

1.1. Cellular Protein Quality Control and the AAA+ Superfamily

Living cells exist in a state of dynamic protein turnover. Proteins misfold due to thermal stress, oxidative damage, or genetic errors; others accumulate to toxic levels or require removal as part of normal cellular regulation. To maintain homeostasis, bacteria have evolved sophisticated quality control systems centered on selective protein degradation. The primary actors of this process are proteases; enzymes that catalyze peptide bond hydrolysis. Examples include, serine, cystein, and AAA+ (ATPases associated with diverse cellular activities) proteases [1]. Among these proteases the AAA+ proteases represent one of the most important and conserved families of protein-degrading machines [2]. AAA+ proteases couple ATP hydrolysis to mechanical unfolding and processive degradation, enabling them to target stable, globular substrates [3]. Phylogenetic analysis reveals that the AAA+ superfamily has diversified into distinct clades, families, and subfamilies (Figure 1.1). Each clade is tailored to unique cellular niches, ranging from mitochondrial membrane remodeling to cytoplasmic stress responses.

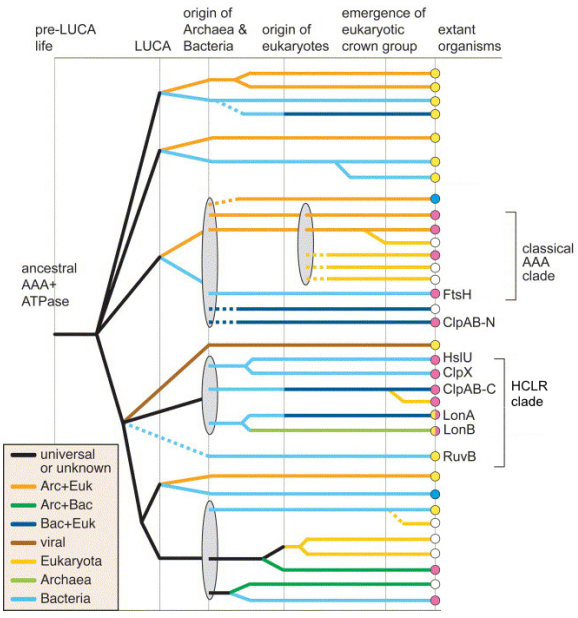

Figure 1.1: Schematic representation of the evolutionary history of AAA+ proteins.
Clades and proteases mentioned in this thesis are indicated. Figure adapted from [4].

AAA+ proteases are characterized by the presence of one or more ATPase domains that form ring-like hexameric [3, 5], or dodecameric assemblies [6, 7]. These ATPase rings are coupled to protease domains or partner proteins to create molecular machines capable of three critical functions:

(1) substrate recognition and specificity, (2) ATP-dependent mechanical unfolding of stable protein structures, and (3) translocation of an unfolded polypeptide chain through a narrow channel where proteolytic cleavage occurs. AAA+ protease examples (Figure 1.2) include the well-characterized ClpXP, ClpAP, HslUV, and Lon proteases in bacteria [2]. These machines are essential for cell survival under stress, for removal of damaged proteins, and for temporal control of cellular processes through targeted degradation of regulatory proteins [8].

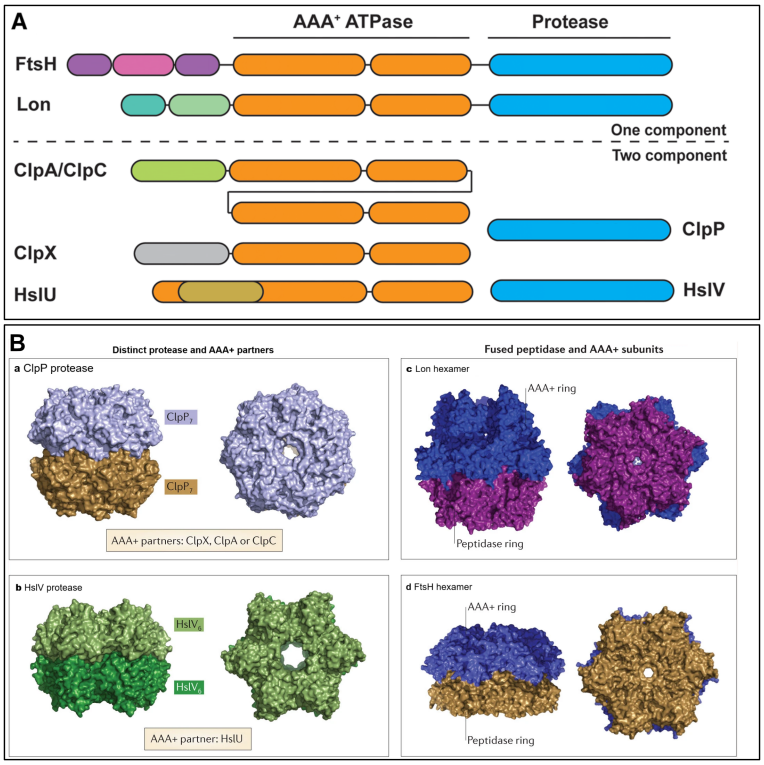

Figure 1.2: Sequence and structure comparisons of distinct and fused protease-AAA+ complexes. **A** | Schematic representation of the domain arrangement of AAA+ proteases in *E. coli*. Sequential homology is shown by similar colours across different domains, distinctions are shown by varying colours. Figure adapted from [9]. **B-a** | The ClpP peptidase from *E. coli* consists of two heptameric rings, and works with either three homohexameric AAA+ partners (ClpX, ClpA, or ClpC). **B-b** | The HslV peptidase consists of two homohexameric rings and partners with an HslU homohexamer. **B-c** | The homohexameric Lon protease is assembled from protease-AAA+ fused module subunits. **B-d** | The homohexameric FtsH protease is built from subunits in which the AAA+ module is fused to the peptidase domain, similar to Lon. Figure adapted from [10].

AAA+ proteases are complex enzymes. They are highly regulated machines that must recognize their specific substrates with precision, unfold them through controlled application of force, and degrade substrates processively. Yet, we lack a dynamic understanding of such dynamics. Single-molecule techniques like optical tweezers (OT) can directly measure these forces and kinetics, bridging the gap between static structures and the real-time mechanics that define cellular proteostasis.

Initially, these questions are addressed through ensemble assays (bulk degradation kinetics [2, 11–14], thermal stability measurements [15, 16]), and through structural biology (X-ray crystallography [17–19] and cryo-electron microscopy [6]). Inherent to these techniques, results are averages of populations of molecules and do not capture the dynamics of individual protein-protein interactions or the forces generated during substrate translocation. These individual interactions can be resolved with OT. However, probing protease dynamics at the single-molecule level necessitates its extraction from the native environment. We recognize that local *in vivo* factors (lipid composition, oligomeric state, coupling to the bilayer, molecular crowding) introduce variability in protein behavior. Therefore, an accurate *in vitro* representation of the native state is needed to justify claims based on the data that is gathered from these experiments.

1.2. FtsH: A Unique AAA+ Protease with Emerging Complexity

FtsH (filamentous temperature-sensitive H), occupies a unique position within the AAA+ protease family. Unlike HslUV, ClpXP, ClpAP, and Lon, which are primarily soluble hexameric assemblies [15], FtsH is an integral membrane protein with a single transmembrane helix that anchors its large cytoplasmic domain to the inner bacterial membrane [6]. Membrane integration is not merely a topological feature; it fundamentally shapes the cellular role and mechanistic properties of FtsH [20]. The protease specializes in degrading misfolded or aggregated periplasmic and membrane proteins, making it a primary guardian of membrane protein quality control [21, 22].

The cytoplasmic domain of FtsH comprises a zinc-dependent metalloprotease domain coupled to a hexameric AAA+ ATPase ring [18, 19]. Crystallographic structures have revealed that the protease domain is uniquely positioned compared to other AAA+ proteases (tilted at an angle rather than sitting atop it), shown in Figure 1.3. This may affect how substrates are threaded and cleaved compared to proteases with more canonical geometries [6]. FtsH can degrade proteins bearing the small single RNA-tag (ssrA-tag) (a post-translational degradation signal), but also recognizes substrates through different mechanisms [2, 14, 20]. These mechanisms are governed by a combination of physical and sequence-based determinants, with a primary emphasis on the accessibility and length of unstructured regions rather than strict sequence motifs. For many membrane protein substrates, FtsH requires a cytosolic tail of at least 20 amino acids to initiate degradation [23, 24]. This length requirement likely reflects spatial constraints of the FtsH complex [18], ensuring that the substrate can reach the active site from the membrane surface. Both N- and C-terminal tails can serve as initiation points [23], and FtsH can degrade substrates bidirectionally [20].

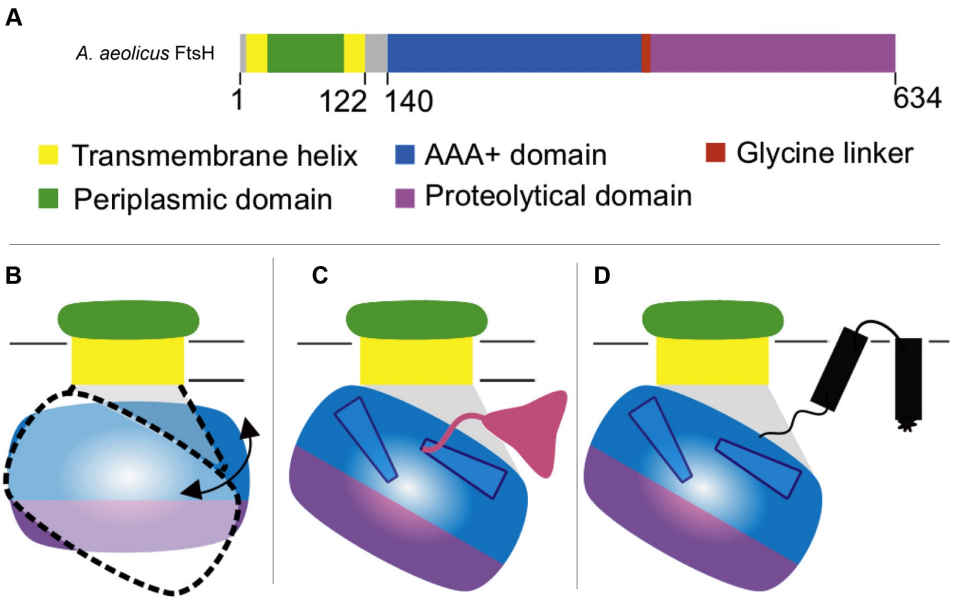

Figure 1.3: Schematic representation of AaFtsH sequence and model for substrate entry.
A | Schematic of AaFtsH sequence with highlighted domains. The periplasmic domain (N-terminal, green) rests between two transmembrane domains (yellow). The second transmembrane helix is followed by an 18 amino acid loop (gray), linking to the AAA+ domain (blue). A glycine linker (red), connects the AAA+ domain to the protease domain (C-terminal, red). **B** | A proposed model [6] for substrate entry. The 18 amino acid flexible linker might allow for the AAA+-protease domain to tilt with respect to in relation to the membrane, creating a 30 Å wide gap that provides access of cytosolic (pink, **C**) and membrane protein substrates (black, **D**) to the central pore in a partially folded state. Figure adapted from [6]

.

In contrast to other AAA+ proteases like ClpXP, which rely on defined sequence tags (degrons) at the N- or C-terminus, FtsH can also recognize internal sequence elements, particularly in partially unfolded or destabilized proteins [14]. For example, studies on dihydrofolate reductase (DHFR) have shown that FtsH does not require an unstructured terminal tail but can instead recognize internal sequences exposed in partially unfolded conformations [13, 24]. This noncanonical recognition expands the collection of FtsH substrates to include proteins that may not present traditional recognition signals, but become susceptible to degradation when they transiently expose internal regions due to

misfolding or stress [24]. Additional research shows that the thermostability of substrates influences degradation rate [14]. FtsH was not able to degrade DHFR-ssrA or Barnase-ssrA. Interestingly, their destabilised mutant variants are degraded by FtsH [25]. These results indicate that FtsH uses protein folding state as a final measure for degradation [20]. In conclusion, an initial generic recognition will first signal FtsH to recognize an array of substrates. Next, substrate stability will determine degradation fate [25]. A damaged or misfolded substrate has lower stability and will be degraded. This dual approach to substrate degradation is how FtsH claims its niche in cellular proteostasis.

What makes FtsH mechanistically intriguing is that it possesses different properties from other well-studied AAA+ proteases. While ClpXP is known for processive, rapid substrate translocation [26–28], FtsH shows evidence of reduced activity [25] and potentially different mechanical force generation [29]. As aforementioned, substrate recognition mechanisms of FtsH differ substantially from those of ClpXP. Yet, despite years of biochemical and structural research, the mechanical dynamics of FtsH activity have never been directly observed at the single-molecule level. In contrast to the detailed single-molecule portraits that exist for ClpXP [26–28, 30, 31], FtsH research shows a significant gap in the mechanistic literature published.

1.3. Protease Mechanics Revealed through Force Spectroscopy

Over the past two decades, single-molecule techniques have improved our understanding of protein-protein interactions and protease mechanics. In particular, OT have emerged as a powerful tool for direct measurement of mechanical forces generated by molecular machines during catalysis [32, 33].

The power of OT for studying proteases lies in several key capabilities. First, by tethering a protein substrate between a trapped bead and a surface-bound protease, one can measure the forces generated as the protease translocates and unfolds the substrate. Second, by recording bead position at high temporal resolution (typically 1–10 kHz), the kinetics of unfolding transitions, force-dependent substrate translocation, and pausing behavior can be observed with high detail. Third, measurements can be conducted under highly controlled conditions (temperature, pH, ionic strength) [32]. Fourth, OT can measure forces at 1–100 pN, a range at which many biological processes operate [33]. In conclusion, OT do not replicate cellular conditions; they can be applied to deconstruct these conditions to reveal the physical laws governing protein machines like FtsH. By quantifying how proteases recognize substrates, generate force, and processively translocate polypeptides at the single-molecule level, mechanistic principles that underpin its cellular roles can be explained.

1.3.1. Principles of Optical Trapping and Force Measurement

An optical trap is formed when a laser beam is tightly focused through a high-NA (numerical aperture) microscope objective. The concentrated region of the focused beam is called the beam waist. The principles through which a particle is trapped in the laser is differ based on the size of the particle ($R_{particle}$). In our case, a 1064 nm trapping laser is used in combination with silica beads at 1000 μm, to which we will restrict our explanation of trapping principles.

The trapping mechanism relies on two competing forces: (1) the gradient force, which arises from the intensity gradient of the focused laser beam which pulls the bead toward the region of highest light intensity at the beam center. (2) the scattering force, which pushes the bead along the direction of laser propagation [33–35] (Figure 1.4). When the bead is positioned off-axis relative to the beam center, the rays closer to the center have a higher insity, transfering more momentum to the bead than those at the edge. This results in a restoring force directed towards the trap center [33, 35, 36]. As the bead reaches the beam center, individual light rays refract through the bead symmetrically, resulting in zero net gradient force and cancellation of the scattering force along the laser beam, allowing the bead to be stably confined in three dimensions [33, 35, 36]. It is important to note that this only holds when the refractive index of the bead is greater than its surrounding medium. If this is not the case, rays will be refracted oppositely, and the bead will experience a force away from the trap center.

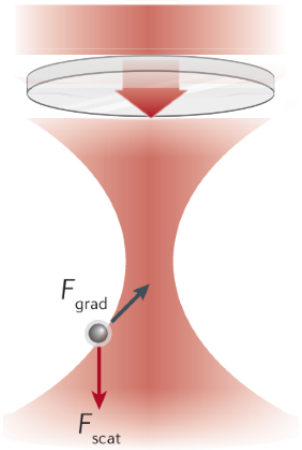

Figure 1.4: Principle of optical trapping for bead of similar size to the laser wavelength. A dielectric particle, such as a silica bead, will experience a scattering force (red arrow) along the propagation direction of the laser beam and a gradient force (gray arrow) that attracts the bead towards the focus. Figure adapted from [33]

The trap stiffness k quantifies the strength of this restoring force: if the bead is displaced a distance Δx from the trap center, the restoring force is in accordance with Hooke's law [37]. The trap stiffness depends on numerous experimental parameters: laser wavelength (λ), laser power (P), numerical aperture of the focusing objective, properties of the trapped bead (size, refractive index, material), and properties of the surrounding medium (refractive index, viscosity, temperature). For biological experiments, k typically ranges from 0.01–1 pN/nm [38]; our experiments employed trap stiffnesses of 0.1–0.2 pN/nm, appropriate for measuring forces in the 1–50 pN range with high spatial resolution.

1.4. The Thermophilic Advantage and Heating Challenge

This investigation of FtsH mechanics required a strategic choice: rather than studying the mesophilic FtsH from model bacteria such as *Escherichia coli*, we otped for the *Aquifex aeolicus* FtsH (AaFtsH) ortholog. *A. aeolicus* is a hyperthermophilic bacterium that thrives at temperatures of 80°C [39, 40]. This choice is motivated by several practical and scientific advantages. First, thermophilic proteins generally exhibit exceptional stability. They remain folded and functional at temperatures that would denature mesophilic orthologs. This enhanced stability has multiple benefits for single-molecule experiments: purified thermophilic proteins aggregate less profusely, have greater resistance to photodamage during laser trapping, and more predictable unfolding/refolding behavior. From a fundamental scientific perspective, the thermophilic variant offers an opportunity to test whether the mechanical principles discovered for mesophilic homologs are universal or whether they depend on organism-specific adaptations.

However, the thermophilic nature of AaFtsH introduces a significant experimental challenge: the enzyme exhibits minimal activity at room temperature and requires temperatures above 50°C (shown in this thesis) for catalytic turnover. This requirement motivated the development and implementation of a heating system for OT, developed by the group [41]. The heating system must satisfy demanding criteria: maintain precise temperature control within a microscopic flow cell, minimize thermal drift and vibration artifacts detrimental to optical trap stability, it cannot obscure the laser path, and it must allow for equilibration to new temperatures without thermal shock to the biological sample. The development and validation of this heating system (built upon prior work in the group [41], from which we have adapted the design) opens new experimental possibilities, as many other biologically important enzymes and proteins are derived from (hyper-) thermophilic organisms or exhibit temperature-dependent activation [25, 42, 43].

1.5. Outline and Organization of this Thesis

The primary goal of this research is to characterize the translocation dynamics of AaFtsH at the single-molecule level and to compare these dynamics with the well-characterized mechanics of other

AAA+ proteases. In order to achieve this goal, we adopted a three-pronged experimental approach:

First, **biochemical characterization and validation** (chapter 3): Before investing substantial effort in technically demanding single-molecule OT experiments, verification of enzymatic activity biology by our AaFtsH is needed. It should degrade physiological substrates under conditions approximating those in the optical trap. We performed degradation assays using ssrA-tagged titin-I27-repeated domains (a mechanical reporter protein widely used in single-molecule studies) and β-casein (an unstructured model substrate). These biochemical experiments served a critical validation function: confirming protein function before proceeding to OT work.

Second, **OT setup calibration and validation** (chapter 4): OT measurements are quantitative only to the extent that the instrument is accurately calibrated. We performed calibration and characterization of our dual-laser OT setup under the specific experimental conditions used for AaFtsH studies, including the elevated temperatures required for enzyme activation. We used 5th-order polynomial fitting to map the relationship between trapped bead position and position-sensing detector voltage, ensuring sub-nanometer accuracy (subsection 4.2.3) in position determination. We characterized how trap stiffness might vary as a function of laser power. Trap stiffness must be known precisely to determine forces accurately. We validated the setup by testing with trapped beads in the optical trap. These validation experiments identified and corrected errors in the pre-existing control software, a process that, while technically challenging, is essential for ensuring the reliability of all subsequent measurements.

Third, **single-molecule OT measurements of AaFtsH-mediated substrate translocation** (chapter 5): With biochemical confirmation of protein activity and comprehensive OT calibration complete, we proceeded to direct single-molecule observations of AaFtsH engaging and translocating ssrA-tagged titin-I27 substrates. We developed an assay in which the substrate is tethered between a trapped silica bead and a surface-bound AaFtsH molecule, and recorded changes in bead position as AaFtsH engaged the substrate and initiated translocation. This assay directly reports on the force dynamics and translocation kinetics of AaFtsH, allowing comparison with the extensive single-molecule literature on other proteases such as ClpXP, ClpAP, and Lon. We performed negative controls; experiments without ATP, in which protease activation should be blocked, to attempt to discriminate between productive substrate interactions and non-specific interactions.

The structure of this thesis reflects this experimental progression: Materials & Methods are explained in detail in chapter 2. The results are presented and discussed in chapters (3–5), each prefaced by an introduction relevant to the results presented, we conclude this thesis in chapter 6. The general introduction (this chapter) provides conceptual framing for all three experimental chapters, emphasizing the broader context of AAA+ protease mechanics and highlighting the specific scientific and methodological innovations of this work. The Conclusions chapter synthesizes findings across all three experimental chapters and discusses implications for future single-molecule studies of thermophilic enzymes and membrane-integrated proteases.

We note at the outset that the single-molecule OT measurements presented in chapter 5, representing the first such study of FtsH, revealed challenging-to-interpret events. This reflects the inherent difficulty of single-molecule experiments on proteases, where interpretable substrate translocation traces are difficult to obtain. We later discuss this challenge in detail; however, we believe that these preliminary single-molecule measurements, combined with our biochemical and instrumental validation, establish foundational work and methodological validation for future studies of AaFtsH and other thermophilic proteases. This work demonstrates the feasibility of heating-enabled OT and opens avenues for applying this novel technique to the growing catalog of thermostable enzymes being discovered and engineered.

2

Materials & Methods

2.1. Biochemical Assays

2.1.1. AaFtsH Purification

E.coli Transformation

C43 *E. coli* cells containing BirA are transformed with pEt22b plasmid (Figure 7.1). Transformation is done through heat shock; keeping 100 μL cells on ice for 30 min. Transfering the cells to 43°C, keeping them on ice again after 90 seconds. The cells are grown at 30°C for 1 hour adding 500μL LB, after which they are centrifuged for 10 minutes at 5000 g. Cells are plated on Amp (ampicillin) containing agar and left overnight at 30°C.

AaFtsH Expression and Membrane Isolation

A single colony is inoculated in 1 L of LB+Amp at 37°C until an OD_{600} (optical density at 600nm) of ~0.6 is reached. The culture is induced by addition of 1 mL 1 M IPTG, and 1 mL 0.1 M biotin. Protein production is done overnight at 18°C. The culture is centrifuged at 4000 g for 20 minutes at 4°C. Next, the cells are dissolved in 10 mL of **lysis buffer** (20 mM Tris-HCl pH 8.0, 300 mM NaCl) per gram of cells. The cells are disrupted three times with a French press at 30 kPa. Unbroken cells are isolated by discarding the pellet after centrifugation for 15 minutes at 24000 g. The membrane fraction is isolated by ultracentrifugation for 4 hours at 125000 g, weighing the membrane fraction (pellet). The membrane fraction is flash-frozen in liquid nitrogen before storage at -80°C for later use.

Affinity and Size-Exclusion Chromatography

When needed, cell membranes are thawed on ice and solubilised in **solubilisation buffer** (20 mM Tris-HCl pH 8.0; 100 mM NaCl; 1% (w/v) LMNG) with a douncer homogenizer, using 100 mL of buffer per gram of cell membrane. The dispersed cell membrane is kept in a tube, keeping it at 4°C for 4 hours on a tube roller for further solubilisation. The cell membrane is diluted 2x, by dripping **dilution buffer** (500 mM NaCl; 40 mM Imidazole) in it, continuously disturbing the solution with a magnet stirrer. Three buffers are prepared in advance; **buffer A** (20 mM Tris-HCl pH 8.0; 500 mM NaCl; 20 mM Imidazole; 5 mM BME (β-mercapto-ethanol); 0.01% (w/v) LMNG), **buffer B** (20 mM Tris-HCl pH 8.0; 500 mM NaCl; 500 mM Imidazole; 5 mM BME; 0.01% (w/v) LMNG), and **Gel filtration buffer** (20 mM Tris-HCl pH 8.0; 150 mM NaCl; 5% (v/v) Glycerol; 5 mM BME; 0.01% (w/v) LMNG). The cell membrane emulsion is loaded on a (previously equilibrated with buffer A) HisTrap 5 mL prepacked column (Ni-NTA Affinity Chromatography). The protein is eluted with a three-step gradient: 15% buffer B, 40% buffer B, 100% buffer B. 280 nm absorbance is monitored in order to decide which fractions to further concentrate. Peak fractions are loaded on a SDS-PAGE gel for analysis, and concentrated to 500 μL using a 30 kDa AMICON filter. The concentrated sample is loaded on a superose 6 10/300GL column, pre-equilibrated with gel filtration buffer. Again, 280 nm absorbance is monitored. Peak fractions are loaded on an SDS-PAGE gel for analysis, and concentrated until ~50 μL with a 30 kDa AMICON filter. The yield is determined with a nanodrop system measuring the 280 nm absorbance.

2.1.2. Titin-I27 Construct Purification

E.coli Transformation

Cultures of *E. coli* BL21(DE3) are transformed with pEt22b plasmid (Figure 7.2, different plasmid for V13P and V15P variants). Transformation is done through heat shock; keeping 100 μL cells on ice for 30 minutes. Transfering the cells to 43°C, keeping them on ice again after 90 seconds. The cells are grown at 30°C for 1 hour adding 500μL LB, after which they are centrifuged for 10 minutes at 5000 g. Cells are plated on Amp containing agar and left overnight at 30°C.

Titin-$I27_4$ Expression and Protein Isolation

A single colony is inoculated in 1 L of LB+Amp at 37°C until an OD_{600} (optical density at 600 nm) of ~0.6 is reached. Substrate expression is induced by addition of 1 mL 1 M IPTG. Expression is done overnight hours at 18°C. Cells are harvested by centrifugation (4000 g for 20 minutes). The pellet is resuspended in **lysis buffer** (50 mM KPi pH 8.0; 1 M NaCl; 5 mM BME; 10% glycerol; 1x Roche protease inhibitor cocktail tablet), and lysed by sonication. The lysate is clarified by centrifugation (18000 g for 45 minutes).

Affinity and Size-Exclusion Chromatography

Three buffers are prepared in advance; **buffer A** (50 mM KPi, pH 8.0; 500 mM NaCl; 20 mM Imidazole; 5 mM BME; 10% glycerol), **buffer B** (50 mM KPi, pH 7.5; 500 mM NaCl; 500 mM Imidazole; 5 mM BME; 10% glycerol), and **Gel filtration buffer** (25 mM Tris-HCl pH 8.0; 150 mM NaCl; 10% Glycerol; 5 mM BME). The supernatant-buffer is loaded on a (previously equilibrated with buffer A) HisTrap 5 mL prepacked column (Ni-NTA Affinity Chromatography). The protein is eluted with a three-step gradient: 15% buffer B, 40% buffer B, 100% buffer B. 280 nm absorbance is monitored in order to decide which fractions to further concentrate. Peak fractions are loaded on a SDS-PAGE gel for analysis, and concentrated to 500 μL using a 30 kDa AMICON filter. The concentrated sample is loaded on a HiPrep 16–60 Sephacryl S-200 HR column, pre-equilibrated with gel filtration buffer. Again, 280 nm absorbance is monitored, peak fractions are loaded on an SDS-PAGE gel for analysis, and concentrated until ~50 μL with a 30 kDa filter. The yield is determined with a nanodrop system at 280 nm absorbance.

2.1.3. Degradation Assay

A **10x reaction buffer** (500 mM Tris-HCl, pH 8.0; 250 mM NaCl; 100 mM $MgCl_2$; 500 μM $ZnCl_2$) is prepared in advance. Samples are thawed on ice from -80°C. The **reaction recipe** (1x reaction buffer; 1 gL^{-1} BSA; 1 mM TCEP; 5 mM ATP; 0.33 gL^{-1} AaFtsH; 0.2 gL^{-1} substrate (titin construct or β-casein)). Reactions are carried out over a temperature range in seperate tubes with a Biorad PCR machine, each tube containing 6 μL of the reaction recipe. A negative control is done by the instantly adding 4 μL 0.5% EDTA (Ethylenediaminetetraacetic acid, AaFtsH inhibitor [44]). The other reactions where eventually stopped through addition of 4 μL 0.5% EDTA as well. 4 μL cracking buffer is added to the reactions before heating them to 95°C for 10 minutes. Next, all reactions are loaded on a SDS-PAGE gel for analysis. The gels are imaged using a ChemiDoc system, and subsequently analysed using ImageJ. To assess degradation, band intensities are normalized to the lowest-temperature condition.

2.2. Setup Calibration & Validation

2.2.1. Building the ITO flow cell

The Indium Tin Oxide (ITO) flow cell is designed by Dr. Roland Kieffer and Chaline Overtoom-van Aartrijk [41]. It consists of a soda-lime glass slide with a thin layer of ITO deposited on one side, two coverslips (22×22×0.15 mm and 15×15×0.10 mm), UV-curing Norland Optical Adhesive 81 (NOA81), silver paint, copper tape, kapton® tape, soldering tin and two electrical wires, see Figure 4.2. This flow cell design allows the insertion of a thin thermocouple. The flow chamber is isolated from the ITO surface.

The flow cell is made by first etching a 40×40×1.1 mm ITO glass (GuangYi Store) with 10×10× mm squares with a laser cutter. Subsequently, the ITO glass is scored with a glass cutter and broken into four equal ITO microscope compatible slides. The ITO slides are cleaned in a glass beaker filled with 3% hellmanex®-III in MilliQ water, sonicating the filled beaker in a sonication bath for 30 minutes.

The hellmanex®-III is removed by rinsing the beaker and ITO slides 5 times with MilliQ water. The beaker is then filled with MilliQ and sonicated for another 30 minutes. Finally, the ITO slides are dried with a nitrogen blow gun and stored in a 50 mL tube until use.

The electrodes are prepared by cutting copper tape (150×5 mm) in half along the long side. Both halves are stuck to a piece of kapton® tape (170×10 mm), both tapes with the adhesive sides against each other. Additionally, wires are soldered to the exposed copper tape. Next, A clean 15×15×0.10 mm coverslip is glued with a drop of NOA81 to the ITO slide, curing the adhesive with a UV lamp during 5 minutes. Two thin lines of silver paint are painted on the ITO layer on either side of the coverslip. The copper/kapton® tape is placed on the silver paint with the copper side on top of the silver paint. The tape combination is longer than the ITO slide width to ensure that wires can be soldered to it. To create the flow cell chamber, double sided tape is folded over itself to create a double^2 (double layered double sided) adhesive. The double^2 adhesive is cut into 17×5× mm strips and stuck to the cover slip on the ITO slide. Finally, the 22×22×0.15 mm cover slip is stuck on top of the double^2 adhesive strips.

2.2.2. Building the Thermocouple

Temperature in ITO flow cell is monitored with a thin thermocouple. A T-type (Cu-Ni) thermocouple with thickness ~80μm is made. This thermocouple measures temperatures in the range -200–200°C with 0.1°C [41] accuracy. The copper (TFCP-003–50, Omega) constantan (TFCC-003–50, Omega) wires are fused together with an electric spark. When desired, the thermocouple can be inserted into the flow chamber, positioned at the midpoint of the flow cell. Due to uniform heating of the flow cell, the temperature within the flow cell will be accurately indicated by the thermocouple [41].

2.2.3. Determining the AOD frequency conversion factor

To determine the conversion factor, relating the AOD frequency in MHz to nm distances, we constructed ITO flow cells as explained in subsection 2.2.1. The flow cell is treated with a **blocking buffer** (50 mM Tris-HCl, pH 8.0; 100 mM NaCl; 10 mM MgAc; 50 μM $ZnCl_2$; 1 mM TCEP; 10% Glycerol; 1 gL^{-1} BSA) to decrease non-specific interactions. We used a 1:1000 (beads:blocking buffer) dilution of 1 μm PolyScience® streptavidin-coated silica beads. The beads are shortly sonicated before dilution. Single beads are trapped with a 10 W, 1064 nm trapping laser at 25% power. The trapping power is attenuated with the AOD, setting $P_{AOD} = 1.8$ mW. The bead position is recorded with a 512×512 pixel resolution ThorLabs® camera. Relative pixel size is calculated with a microscope calibration camera slide. The correlation between AOD frequency and nm distance is determined by changing the AOD frequency (24–28 MHz), while recording the bead position of a trapped bead with the camera. The bead position in pixel distances is calculated by image analysis in ImageJ, converting these distances into nm with the obtained data from the calibration slide. The X, and Y, conversion factors for AOD frequency to nm distances are determined with a linear regression.

2.2.4. Trap stiffness experimentation & Allan Variance Analysis

To investigate whether we could obtain reproducable trap stiffness across multiple experiments to measure forces within relevant ranges, we constructed ITO flow cells as explained in subsection 2.2.1. The flow cell is treated in the same fashion as subsection 2.2.3, with the same beads and laser setting. To investigate trap stiffness, we attenuated the AOD, setting the AOD power to 0.2–1.0 mW. The flow cell is heated through application of a DC voltage to the electrodes. Each flow cell required different voltages, but in general around ~16–18 V is sufficient for heating the flow cell to a desired temperature of ~50°C. For both trap stiffness experiments and AV analysis, beads are trapped in the middle of the flow cell and bead position is recorded at 10 kHz sampling rate for 10 seconds. The trap stiffness is determined through corner frequency analysis as described in subsection 7.2.1. The AV plots are generated by plotting the positional variance of the bead over a range of timescales as multiples of 2 from the sampling rate. From the AV analysis, the gaussian white noise regime is deterimened with a linear fit to the logarithmically transformed AV ($\log(\sigma_\tau^2) = m \cdot \log(\tau) + c$). Here, m represents the slope, τ the averaging time, and c the intercept. The white noise regime is defined as the region where the slope satisfied: $m \in [-0.8, -1.2]$. The sampling rate which ensures the highest spatial resolution is selected from this domain as the resampling frequency for raw data.

2.3. Optical Tweezer Experiments

2.3.1. AaFtsH surface immobilisation in the flow cell

Flow cells are constructed as described in subsection 2.2.1. Buffers and fluids are flowed through the flow cell by pipetting a drop on one side of the opening, and inducing flow with a kimtech® tissue. First, the flow cell surface is incubated for 1 hour with a 200x dilution of streptavidin (SA) (SA-Cy5, Invitrogen™) in blocking buffer. The flow cell is washed with blocking buffer and incubated with blocking buffer for 1 hour. The purified AaFtsH (described in subsection 2.1.1) is diluted to ~100 nM with blocking buffer. AaftsH is immobilized on the surface by flowing the AaFtsH dilution into the flow cell, incubating in a 4°C fridge for 1 hour.

2.3.2. Preparation of Titin-beads

To construct the substrate construct (Figure 3.2) a 3500 base-pair DNA linker is constructed by PCR using M13mp18 plasmid as a template, one oligonucleotide primer with a 5'biotin, and a second oligonucleotide primer containing a 5'amino group. DNA-HaloTag oligonucleotide are ordered (Promgea) and directly used in PCR. The multidomain titin-I27^{VxP} is purified as described in subsection 2.1.2. The Titin-I27^{VxP} is linked to the halogenated by incubating a **DNA-titin recipe** (264 nM DNA linker; 1.6 gL^{-1} Titin-I27^{VxP}; 1x reaction buffer) for 3 hours at room temperature.

Titin-beads are prepared by incubating the **bead recipe** (1x reaction buffer; 0.4 gL^{-1} BSA; 2 μL PolyScience® streptavidin-coated silica beads; 2 μL DNA-titin recipe; 2.5 mM TCEP) at room temperature for 2 hourse. The silica beads are sonicated before addition to the bead recipe. After incubation, the beads are spun down for 1 minute at 12000 g and resuspended in 50 μL blocking buffer 3 times.

2.3.3. Optical Tweezers Experimentation

A surface immobilized AaFtsH ITO flow cell is made according to subsection 2.3.1. The washed bead recipe from subsection 2.3.2 is diluted 300x, 200x, and 100x in **ATP buffer** (1x reaction buffer; 5 mM ATP; 1 mM TCEP; 0.05 gL^{-1}). Different dilutions are added in descending order, keeping the visually best dilution in the flow cell. The thermocouple (subsection 2.2.2) is added to the flow cell. Either openings of the flow cell are closed with grease to allow for a closed system, with the ability to expand as the flow cell is heated. A DC voltage is applied with 1 V min^{-1} increase until 50°C is reached. It is important to gradually build temperature, as aggregates seem to form when temperature increases rapidly.

Before initiation of substrate engagement by AaFtsH, free beads are trapped with the trapping laser (Figure 4.1). Trap stiffness is determined through corner frequency analysis (subsection 7.2.1). Position calibration is done by raster scanning. Beads are axially scanned with a piezoelectric stage to determine the location of the flow cell surface. Beads are scanned across the surface in a stepwise manner (20 nm s^{-1}), while monitoring the bead position relative to the trap. When a signal change is recorded (bead moving out of the trap center) the measurement is initiated. Bead positions are recorded at 10 kHz, anti-aliasing filtered at 5 kHz, with an AOD in position-clamp mode to maintain a stable frame of reference. Data is processed based on AV-guided resampling (subsection 4.2.3). Data is fitted with the AVKV step-fitting method.

3

Biochemical Characterization and Validation of Purified AaFtsH

3.1. Introduction

3.1.1. From Gene to Functional Protein

The journey from DNA sequence to active protein is a multi-step process. While routine for soluble proteins, more challenges are present for integral membrane proteins[43]. In particular, proteolitically active enzymes must be handled carefully to prevent self-degradation. AaFtsH, a membrane-integrated AAA+ protease, sadly complies to both prerequisites. Our research requiers us to successfully express full-length AaFtsH in *E. coli* (a mesophilic host) and subsequently purify it in a form that retains full enzymatic activity. This chapter validates that purification, confirming that the protein we use in OT experiments (chapter 5) is functional and maintains the catalytic properties expected of native AaFtsH.

3.1.2. Expression and Purification of Thermophilic Membrane Proteins in Heterologous Hosts

Expressing a thermophilic protease (AaFtsH) in a mesophilic host such as *E. coli* is not straightforward. While thermophilic proteins are stable at lower temperatures, successful heterologous expression requires that the mesophilic host cell can tolerate the presence of the foreign protein. Some thermophilic proteins aggregate when expressed at the normal growth temperature of *E. coli* (37°C) because the host's chaperone systems are not fully adapted to recognize and fold thermophilic sequences [45]. Additionally, if the expressed protein is catalytically active it may degrade host proteins or aggregates, potentially impairing host cell viability. Purifying thermophilic FtsH orthologs [18] while retaining its catalytic ability has been shown [6], and we will make informed decisions based on these results.

Our expression strategy employed a plasmid-based (pET22b, shown in Figure 7.1) system in which the AaFtsH sequence is placed under the control of an inducible promoter, allowing for controlled expression during late-stage bacterial growth. The resulting AaFtsH protein, overexpressed in *E. coli*, retains its thermophilic signature: a full-length membrane protein with a single transmembrane helix that anchors it to the inner membrane, a biotin-modification that permits surface-immobilization for OT experiments, a C-terminal His-tag, an Avi-tag, and full proteolytic activity. The His-tag is needed for affinity chromatography purification. The Avi-tag is used in combination with BirA (Biotin Protein Ligase) for post-translation biotynilation of AaFtsH [46, 47]. However, expression is just one of the hurdles. Purification of membrane proteins is difficult due to their poor solubility in aqueous buffers. As a result, membrane proteins tend to aggregate during final isolation steps.

This thesis builds on previous work [6, 41], from which the purification protocol is adopted. The membrane fraction is solubilized in a mild detergent (LMNG; (Lauryl Maltose Neopentyl Glycol), selected to minimize protein aggregation), a strategy suitable for membrane proteases. AaFtsH is enriched further by affinity chromatography (exploiting the added His-tag), and subsequently

undergoes SEC (size-exclusion chromatography), after which the yield is determined with a nanodrop system. Proteolytic activity is validated through the degradation assays described below. Critically, we note that the purified AaFtsH exists as a detergent-solubilized membrane complex in our biochemical preparations. While this differs from the protein's native state (integrated into a lipid bilayer), it provides sufficient stability and activity for both biochemical assays and OT experiments, where the protein is immobilized on a glass surface via a streptavidin-biotin bond.

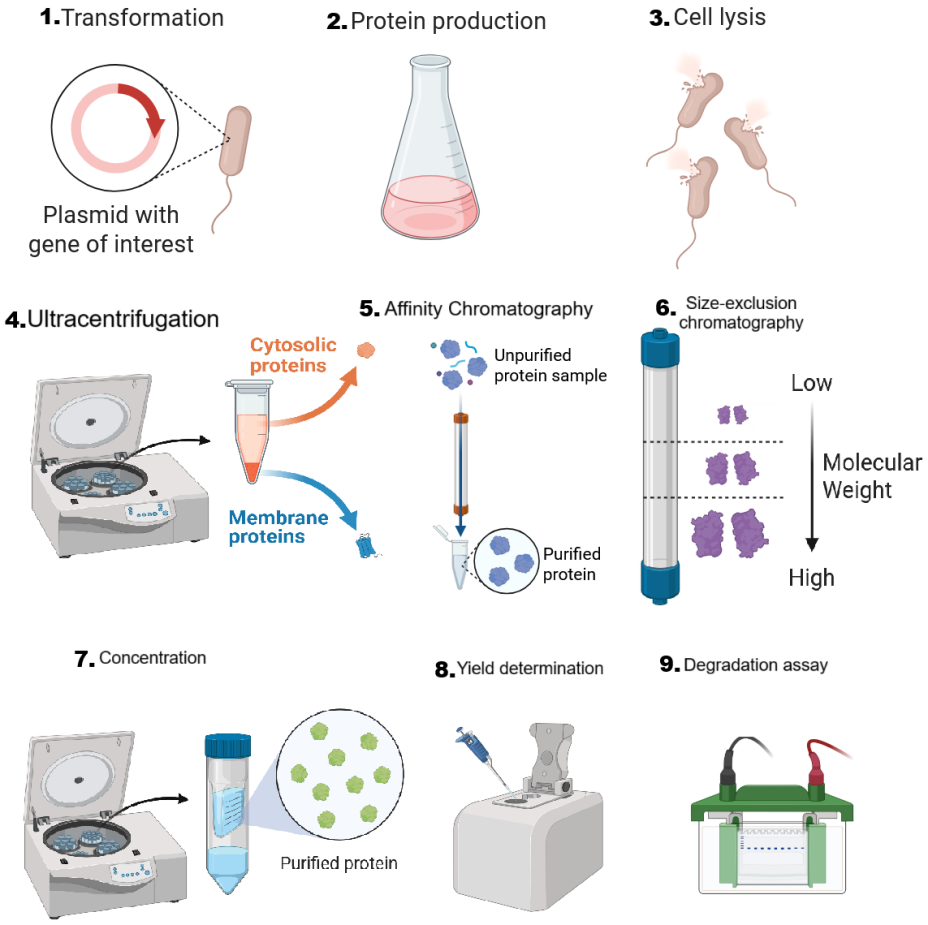

Figure 3.1: Schematic representation of protein purification workflow.
From left to right, top to bottom, *E. coli* is transformed with pET22b plasmid, protein production is induced with IPTG. Cells are lysed with a french press system, after which the membrane proteins are seperated from the cytosolic proteins through ultracentrifugation. Either fraction is kept based on titin/AaFtsH purification. The protein is purified in two steps: Affinity chromatography (to the C-terminal His-tag on the protein), and size-exclusion chromatography. Next, the fractions of interest are concentrated. Protein content is determined with a nanodrop system, after which a degradation assay is performed to determine protein activity.

3.1.3. Degradation Assays as a Golden Standard for Protease Validation

An important step in our methodology is the verification that our purified protease is actually active before we proceed to single molecule experiments. The most direct method is a bulk degradation assay: incubate the purified protease with a defined substrate in the presence of ATP and cofactors, while monitoring substrate disappearance based on parameters that need investigation. We implemented negative controls with use of Ethylenediaminetetraacetic acid (EDTA), a known functional inhibitor to FtsH [43]. We characterized how AaFtsH activity varies as a function of temperature (measuring degradation rates at temperatures spanning the physiological range for *A. aeolicus* and functional range of our OT heating system). These characterizations serve two purposes: (1) they provide verification of succesful purification, and (2) they characterize the temperature dependence of enzyme activity in the temperature range (40–60°C) our OT setup is limited to.

We employed different types of model substrates during the degradation assays, each serving a different purpose:

1. ssrA-tagged titin-I27-repeated domain as a mechanical reporter: The I27 domain is the 27th immunoglobulin-like domain from the giant muscle protein titin. It is ~90 amino acids in size, forms a stable β-sandwich fold, and is commonly used as a mechanical reporter in single-molecule studies as it unfolds at well-characterized forces (150–200pN at physiological conditions [48–50]). The titin-I27 domain is used often as a model substrate in OT studies on AAA+ proteases [26, 28, 51, 52]. Different point mutations (V13P, V15P) destabilize the titin-I27 domain [50]. Mutants V13P and V15P show reduced unfolding forces (-72 and -45pN respectively), compared to wildtype Titin-I27 [53]. The choice of Titin variants allows for systemic interrogation of protease activity against substrates with differing stabilities. Monitoring the degradation of substrates via SDS-PAGE (sodium dodecyl sulfate-polyacrylamide gel electrophoresis) provides qualitative data on protease activity. The use of I27 is particularly strategic for our work because it allows for direct comparativity between the results presented in this thesis and the widely documented characteristics. Logically, this substrate will be used in our subsequent sinlge molecule experiments (chapter 5), ensuring that our biochemical proof-of-concept is directly relevant to our OT measurements.

To probe the mechanochemical activity of FtsH at the single-molecule level, we designed a polyprotein substrate consisting of a HaloTag-I27$_4$-His$_6$-ssrA construct (Figure 3.2). The HaloTag, enables site-specific attachment of the substrate to DNA handles. The C-terminal ssrA tag (AANDENYALAA), a degradation signal recognized by AAA+ proteases [26, 28, 30, 51, 52], serves as the targeting motif for FtsH-mediated unfolding and proteolysis. This tag ensures that FtsH engages the substrate in a physiologically relevant manner, mimicking its natural role in protein quality control. The tandem repeats of the titin I27 domain serve a critical function: The I27 domain unfolds with a distinct extension (~11nm [54]), providing a signature that allows clear verification of FtsH-mediated unfolding via changes in contour length. The repeated I27 modules act as a *molecular ruler*. As FtsH translocates and unfolds each I27 domain, the stepwise increase in end-to-end distance can be resolved with precision, enabling quantification of unfolding kinetics, processivity, and force-dependent pausing. Finally, the hexahistidine (His$_6$-tag) facilitates affinity purification via Ni-NTA chromatography. This modular design, provides a robust platform to investigate the mechanisms of FtsH-mediated proteolysis under force.

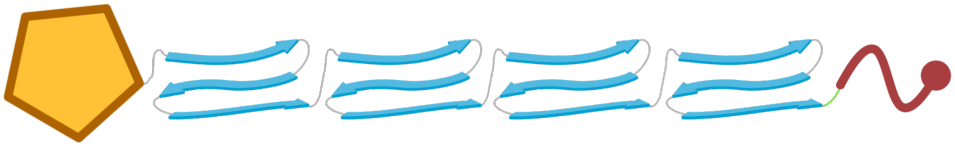

Figure 3.2: Schematic of the polyprotein construct used as model substrate.
The from left to right, or N- to C-terminus, the construct consists of a HaloTag (yellow), tandem I27 repeats (blue), the His-Tag for affinity purification (green), and the ssrA tag (red) for recognition by AaFtsH.

2. β-Casein as a model substrate: β-casein is a flexible, unstructured milk protein, used as a classical model substrate for proteases. Unlike the structured I27 domain, β-casein does not require mechanical unfolding by the protease; it is already disordered and is rapidly degraded by proteolytically active proteases. β-casein degradation assays are less mechanistically informative than titin assays, but provide a rapid, simple validation that the protease is catalytically competent. We performed β-casein degradation assays as an additional check on AaFtsH activity, before moving on to titin as a substrate, as β-casein is more readily available.

3.2. Results and Discussion

Here, we present results from our degradation assays, characterizing AaFtsH activity on both I27-ssrA and β-casein substrates, exploring temperature modulates degradation. We discuss what our biochemical data reveal about AaFtsH function, and how our biochemical findings inform the methodology of OT experiments.

To ensure that the detergent-solubilised AaFtsH retained its unfoldase and proteolytic activity after purification, we evaluated its substrate degradation ability across two temperature ranges: (**1**) Physiological temperatures (54–74°C), reflecting the *A. aeolicus* native thermophilic environment,

and (**2**) Optical tweezers-compatible temperatures (45–65°C), necessary to determine if AaFtsH shows functionality for subsequent force spectroscopy experiments.

3.2.1. AaFtsH Retains Activity at Physiological Temperatures

We first assessed proteolytic activity of AaFtsH at thermophilic temperatures (56–74°C) with the aforementioned model substrates: Titin-I27 variants (V13P, V15P) and β-casein. Analysis of SDS-PAGE gels (Figure 3.3A) demonstrates temperature-dependent degradation of all substrates. Quantification of band intensities (normalized to the lowest temperature condition; Figure 3.3B) revealed two key observations: First, AaFtsh shows progressive degradation of its substrates with increasing temperature, reaching ~40% degradation at 74°C compared to its activity at 56°C for both mutated titin variants. This trend aligns with prior reports of FtsH unfoldase activity against stable substrates [13, 14, 23, 55], where thermal destabilization of titin-I27 likely facilitates processive translocation [25]. Additionally, our AaFtsH shows progressive degradation of β-casein, reaching ~90% degradation at 74°C compared to its activity at 56°C. This is consistent with FtsH's ability to target intrinsically disordered proteins without requiring mechanical unfolding [6, 42, 56]. Laslty, we found that our detergent-solubilised AaFtsH is able to self-degrade, which is consistent with published literature [42, 43]. Self-degradation reached reached ~40% at 74°C compared to its activity at 56°C, similar to the degradation of titin variants. This result further underscores the ability of AaFtsH to digest stable substrates. These results together demonstrate that detergent solubilised AaFtsH retains activity and substrate degradation under thermophilic conditions. We do note that these experiments serve as a qualitative indication that our purified, detergent solubilised AaFtsH is in working order for subsequent experimentation. Investigation of kinetic parameters are beyond the scope of this research and should be determined with more accurate experimentation.

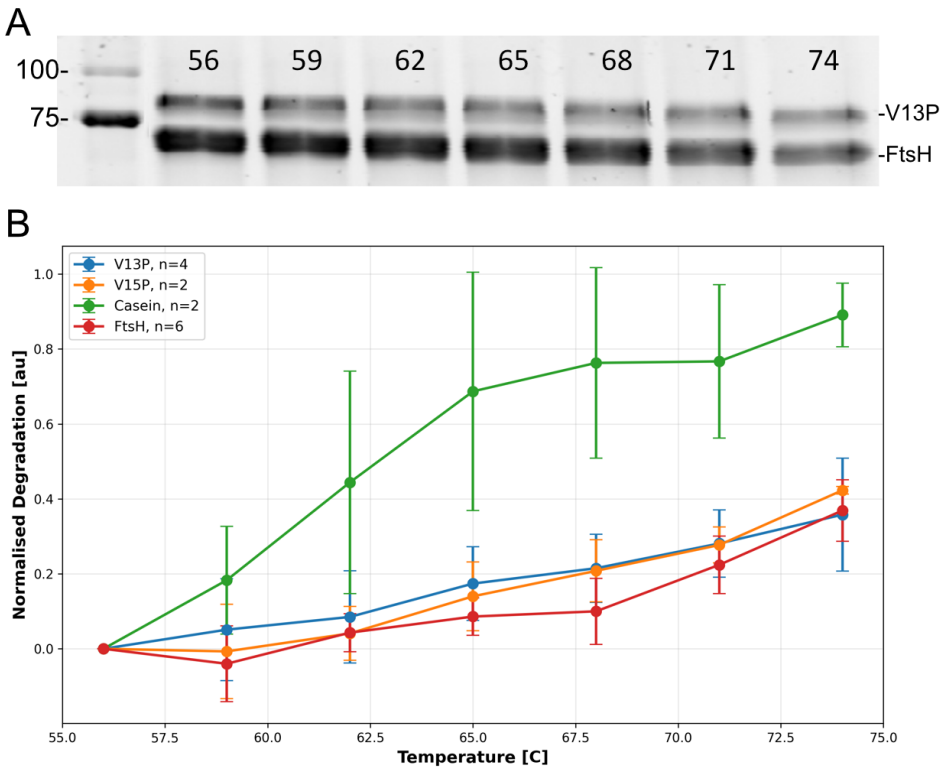

Figure 3.3: FtsH degrades model substrates at physiological temperatures.
A | Representative SDS-PAGE gel showing (l.t.r) a protein ladder in kDa, degradation of titin-V13P, and FtsH by immobilized FtsH at 56–74°C, indicated per band. **B** | Quantification of substrate degradation (normalized to 56°C; average ± SD) for Titin-V13P, Titin-V15P, β-casein substrates, and self-degradation by FtsH.

3.2.2. FtsH Remains Catalytically Active at OT Temperatures

While AaFtsH is thermophilic, our heated single-molecule OT system is limited to a temperature of 55°C to minimize thermal drift and maintain instrument stability. We thus tested if our AaFtsH shows is catalytically active against titin-V13P and β-casein as substrates in a temperature range of 40–70°C. Despite the lower temperatures, we observed that degradation of both substrates increased progressively with increased tempereature. Degradation of Titin-V13P by AaFtsH seems to plateau at temperatures above 60°C (Figure 3.4), reaching ~55% from 60°C compared to its activity at 48°C. The degradation curve of β-casein has similar features, reaching ~80% degradation at 60°C compared to its activity at 42°C. Additionally, the curves in Figure 3.4 show a clear increase in activity by AaFtsH from 50°C for both substrates. Due to the thermophilic nature of *A. aeolicus* [39, 40], the optimum temperature of AaFtsH should be around 80°C. The results from Figure 3.3 and Figure 3.4 indicate that our AaFtsH is active at lower temperatures, where activity increases with temperature. While autoproteolysis clearly occured at high temperatures, it is not directly noticeable in the gels under the lower temperature conditions.

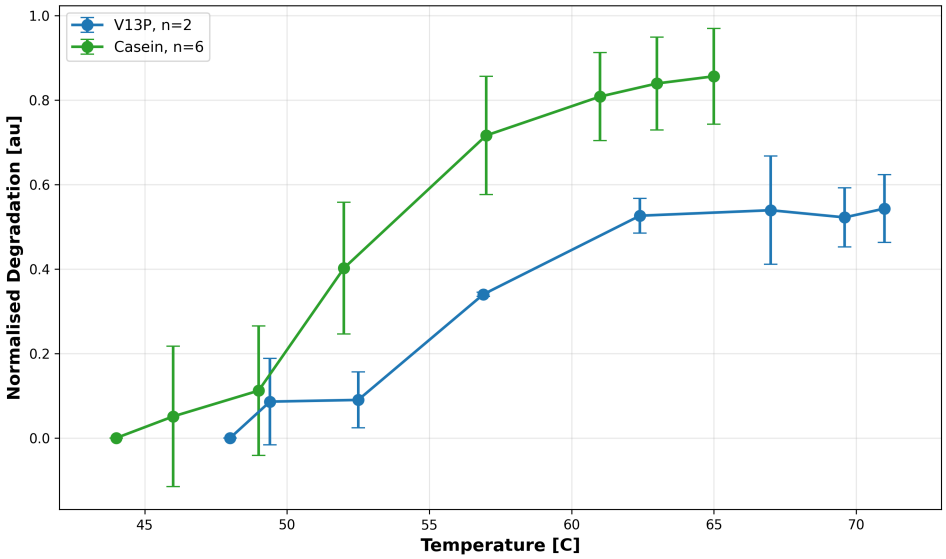

Figure 3.4: FtsH degrades model substrates at the OT system temperature range.
Quantification of substrate degradation (normalized to the lowes temperature; average ± SD) for Titin-V13P, and β-casein substrates.

These experiments served to validate the functional integrity of our purified, detergent solubilised AaFtsH and confirm its substrate degradation under both physiological and experimental conditions. These results demonstrate that AaFtsH activity is sufficient for OT assays. Critically, the temperature-dependent (auto-) proteolysis observed here aligns with prior research [25, 42, 43], where self-degradation is proposed to regulate protease levels under stress. Its negligable occurence to Titin-V13P suggests that conformational stability is maintained under our experimental conditions. This stability is critical for single-molecule assays, where enzyme longevity directly impacts data quality. With this validation complete, we next move on to validation of our OT system.

4

Calibration and Validation of Dual-Laser Optical Tweezers at Elevated Temperature

4.1. Introduction

4.1.1. The Quantitative Obligation in Single-Molecule Measurements

Single-molecule experiments lack averaging inherent to bulk biochemical assays. When we measure the motion of a single protein or a protein-tethered bead, the measured value is the data point of interest. The opportunity for averaging many identical trials and invoke statistics to reveal a hidden signal does not exist. Consequently, single-molecule experiments impose rigorous demands on instrumental calibration and validation. Any systematic error introduced during calibration will directly translate into errors in the biological conclusions. This principle is particularly acute in OT experiments, where the relationship between bead displacement and trapping force follow Hooke's law [37] ($F = k\Delta x$), a proportionality that is only valid if the trap stiffness k is accurately known and constant over the experimental conditions employed.

This chapter describes our approach to validating our OT setup in preparation for single-molecule measurements of AaFtsH. The work is motivated by several considerations: (1) our dual-laser OT system, inherited from prior research [41], required re-validation and -calibration after some years of use; (2) the addition of a heating system seemed to enhance protein aggregation [41], maybe due to thermal instability or drift (which can also change optical properties) which needs characterization; and (3) small discrepancies discovered in the measurements, led us to find errors in the pre-existing code which needed system-wide correction to ensure accuracy.

4.1.2. The Optical Tweezers Setup

The setup used for this thesis has been built previously [41] for a dual-trap optical setup. A single laser beam (1064 nm) is split into two, based on polarization, to allow for two simultaneously present optical traps [33, 57]. The 1064nm wavelength is particularly advantageous for biological applications because water has a low absorption coefficient at this wavelength, minimizing photodamage to the sample [36, 58, 59]. For our experiments, a single trap (Figure 4.1) is used. Therefore, one of the split laser beam paths is blocked. The lenses in the optical setup are set to a 4f-arrangement (lens seperation based on the sum of focal lengths). The beam diameter and collimation of the beam have been verified previously [41]. An acousto-optic deflector (AOD) is used for precise control of the trapping laser focus. The AOD accepts a high-frequency input (in our case, the trapping laser is centered at 26 MHz). Varying the input frequency will deflect the trapping laser and change the position of the trap.

To allow for precise location of the trapped bead, a position sensing detector PSD in combination with a distinct detection laser (830 nm). The PSD outputs electrical signals proportional to the position of the detection laser spot at high temporal resolution (up to 50 kHz sampling rate). The

output voltage from the PSD is linearly proportional to bead position over a range of several hundred nanometers. Through measurement of PSD voltage, the bead position can be determined. Through carful determination of the trap stiffness k, the bead displacement Δx can be converted into force with Hooke's law. Consequently, the accuracy of force measurements depends critically on two factors: (1) accurate calibration of the relationship between PSD voltage and true bead position, and (2) accurate determination of trap stiffness.

Additionally, the OT setup is equiped with a piezoelectric stage. Computer controlled software allows us to move the sample with high accuracy in X, Y, and Z directions.

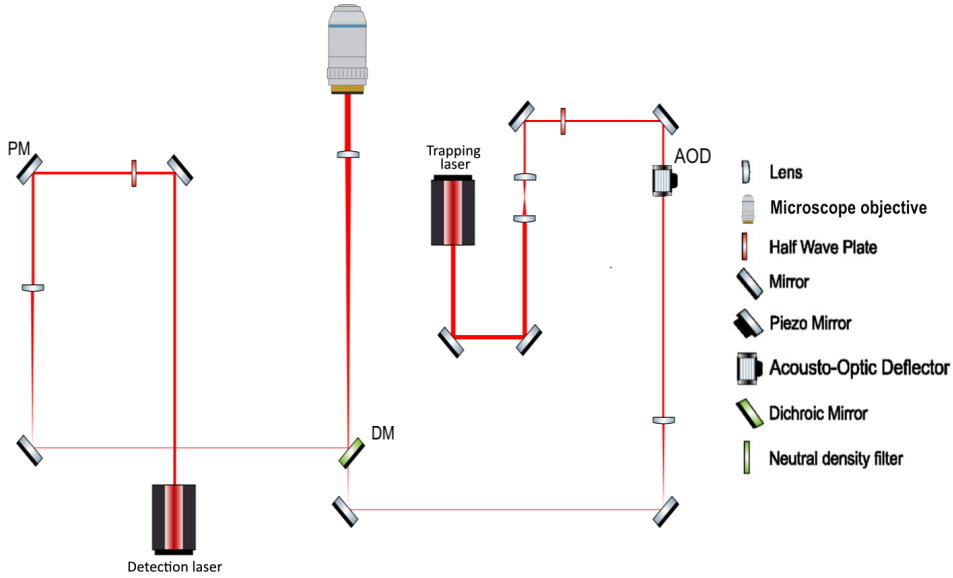

Figure 4.1: Schematic of the optical components. The trapping laser (1064nm) is aligned with an AOD to allow for precise location of the trapping laser focus. The detection laser (830nm) is combined through a dichroic mirror and focused by a high NA microscope objective. Only the beam paths used for a single optical trap are shown. The lenses are configured to a 4f arrangement. Figure adapted from [41]

4.1.3. Calibration Methods: From Static to Dynamic Approaches

Static calibration (polynomial fits): Our primary calibration method employed a static approach: the bead is scanned through a grid around the trap focus by varying the input frequency to the AOD. The PSD voltage is recorded at each position. The results of the voltage-position relationship are fitted to a quintic polynomial (Equation 4.1, Equation 4.2). This calibration curve maps PSD x- and y-voltage to a corresponding bead position in MHz, as posed by the AOD. Fitting will yield the coefficients (A_{ij}, B_{ij}) that establish the correlation between AOD frequency in MHz and PSD voltage. This approach is already implemented for the OT system and is the standard method used in our optical tweezers setup. The bead position in MHz can be translated into nanometer through another calibration between AOD frequency and distance. Each bead is calibrated before measurement as variances in bead size and sphericity can influence the position of the trapped bead.

$$F_x(V_x, V_y) = \sum_{i=0}^{5} \sum_{j=0}^{5-i} A_{ij} V_x^i V_y^j \tag{4.1}$$

$$F_y(V_x, V_y) = \sum_{i=0}^{5} \sum_{j=0}^{5-i} B_{ij} V_x^i V_y^j \tag{4.2}$$

Trap stiffness determination: Corner frequency analysis: The trap stiffness k is mainly determined using the frequency-domain properties of the trapped bead. When a bead is trapped in a harmonic potential well, it undergoes thermal motion with a characteristic timescale determined by the balance between the trapping force (proportional to k) and viscous drag η from the surrounding medium. The power spectral density (PSD) of position fluctuations exhibits a characteristic corner

frequency (subsection 7.2.1). By measuring bead position at high temporal resolution (10 kHz sampling frequency during our experiments), we can quantify the PSD of the signal. We can identify the corner frequency and, knowing η, extract k. The advantage of this method shows as it requires no moving parts and can be applied while a free bead is trapped. Similar to positional calibration, the trap stiffness is determined for each bead independently.

4.1.4. Temperature-Dependent Optical Tweezers: New Challenges and Solutions

Our experiments required heating the optical tweezers flow cell to >50°C for AaFtsH to show degradation ability of the model substrate (Figure 3.4). While this heating is biologically necessary, it introduces several technical challenges absent in room-temperature optical tweezers:

Thermal drift and vibration: Heating causes inhomogeneous thermal expansion of the optical elements, flow cell, and microscope stage. In non-uniform expansion, the focal point of the laser point can be altered, resulting in a trap center drift relative to the flow cell. Drift of even a few nanometers over the course of an experiment will corrupt data. Additionally, heating can introduce vibrations from thermal convection. Even more, increased temperatures increase thermal noise. These effect together degrade position measurement accuracy and stability. These effects are mitigated through careful flow cell design ensuring uniform heating.

We adopted the flow cell design developed by the group, which uniformly heats the sample [41]. The design (Figure 4.2) achieves uniform heating through an ITO (Indium Tin Oxide) coated glass slide. The ITO coating will act as a resistor when a voltage is applied, generating heat. A thermocouple can be placed in the ITO flow cell to monitor local temperature.

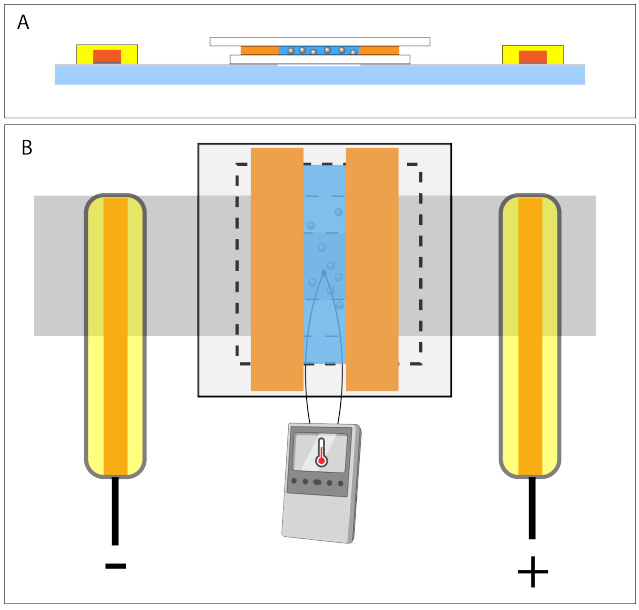

Figure 4.2: Schematic representation of the ITO-Flow Cell. a | Side view of the flow cell. The flow cell is built from an ITO (light grey) coated glass (light blue). A voltage can be applied by silverpainting (dark gray) either side of the ITO slide on one face, to which copper (dark orange) and heat endurance tape (yellow) are stuck. The channel (blue) is created by glueing two cover slips (white) seperated double-sided tabe (orange). **b** | Top view of the flow cell. Additionally, wires (black) and the thermocouple are shown.

4.1.5. Setup Validation: Confirming Accuracy and Discovering Software Errors

Before using our optical tweezers setup for actual biological measurements, we validated its calibration and operation through several tests:

Trap stiffness investigation: We performed multiple independent measurements of trap stiffness at fixed AOD power and temperature. These test are done to get a better understanding of the system, confirming that the values are reproducible. Additionally, this test is done to assure that we are able to use the system for SM-OT experiments, yielding trap stiffnesses relevant for biological measurements with biological measurements.

Allan Variance analysis: This provides a quantitative framework for determining the optimal

sampling rate (f_s) for our OT measurements [60, 61]. We acquire data at high frequency (f_s = 10 MHz), capturing a high bandwidth of positional information available in our OT setup. The Allan variance (AV) is then calculated across a range of observation times (τ) as multiples of 2 from $\frac{1}{f_s}$ sampling period, revealing how measurement accuracy varies with timescale [60, 61]. The minimum in the AV curve identifies the optimal observation time where thermal noise and drift effects balance most favorably, directly indicating the positional accuracy achievable at suteh given timescale [60]. Additionally, AV analysis can give insight into different noise types present in the system [61].

Most single-molecule optical tweezers studies of AAA+ proteases have been performed at room temperature [26, 28]. Our high-temperature measurements of thermophilic FtsH requiers careful noise characterization to ensure us that our setup achieves comparable positional resolution despite the 20% increase in thermal fluctuations. This analysis serves as a robust verification that our system operates at an accuracy sufficient for resolving steps at the nanometer scale.

It is important to note that it is possible that the optimum in positional accuracy might be at a timescale not compatible with the timescale of FtsH dynamics. From this AV curve, we can however derive a timescale at which sampling rate is balanced with positional accuracy to resolve individual steps during substrate translocation by FtsH. Once a balanced observation time is identified from the AV analysis, the high-frequency data can be digitally resampled to match the optimal sampling rate for subsequent analysis of dynamics [60].

Software verification and error correction: During initial AaFtsH OT experimentation, we noticed systematic discrepancies in the measured bead position. This led us to revalidate the system by investigating how bead position changed when the piezoelectric stage is moved to known positions over given time intervals. The dragforce experienced by a trapped bead due to movement of the stage was modeled in Python to determine if the output of the computer position calibration software for the OT setup is correct. This led us to identify errors in the pre-existing bead position conversion software. These errors led to systematic errors in the determination of the true bead position. While discovering these errors was unexpected and required substantial troubleshooting, correcting them was essential for ensuring measurement accuracy. A critical section of the software was re-implemented, and calibration of the system after these corrections is completed.

4.2. Results and Discussion

Now we present our results on system calibration, Allan variance analysis, trap stiffness stability, and position modeling of the system. These results are discussed in light of requirements for our single-molecule measurements and compared to relevant literature.

4.2.1. AOD Spatial Calibration

The AOD frequency-to-position calibration yielded a highly linear relationship ($R^2 > 0.999$, supplemental Figure 7.5), with a conversion factors $\alpha_x = 1089.03 \pm 5.6$ nm/MHz, and $\alpha_y = 1119.25 \pm 5.5$ nm/MHz (mean $\pm$ SD, $n = 4$ measurements). The relative uncertainty of ~0.5% in the conversion factor enables accurate distance measurements throughout OT experiments. The high linearity across the measured range (24–28 MHz) in both directions confirms that the AOD is stable and suitable for precise nanometer-scale positioning. The obtained calibration factors ($\alpha_1 x, \alpha_y$) are subsequently applied when calculating all bead positions.

4.2.2. Trap stiffness reproducability

To establish the relationship between AOD power and trap stiffness, we characterized the optical trap stiffness as a function of AOD RF power using corner frequency analysis (subsection 7.2.1). As expected, the trap stiffness increases with AOD power, though the relationships exhibits moderate scatter ($r^2 > 0.85$), particularly at high AOD power (Figure 4.3). This variability likely reflects day-to-day fluctuations in laser alignment and thermal stability at elevated temperature rather than systematic optical effects. Importantly, the detection laser did not contribute measurably to optical trapping, as confirmed by the inability to trap beads using the detection laser alone.

Despite the moderate correlation, the power-stiffness chapacterisation demonstrates that our system provides tunable trap stiffness spanning 0.02–0.20 pN nm^{-1}, a range compatible with established single-molecule optical trapping studies of protein unfolding and translocation [33, 59]. This tunability enables optimization of trap stiffness for specific experimental requirements:

lower stiffness (0.05–0.10 pN nm^{-1}) provides enhanced force sensitivity for detecting weak protein-substrate interactions, while higher stiffness (0.15–0.20 pN nm^{-1}) improves tether stability during extended measurements. As FtsH translocation has not yet been properly characterised, we selected a range of trap stiffnesses of (0.05–0.15 pN nm^{-1}) by modulating AOD power. Through this approach we try to balance force resolution against tether longevity.

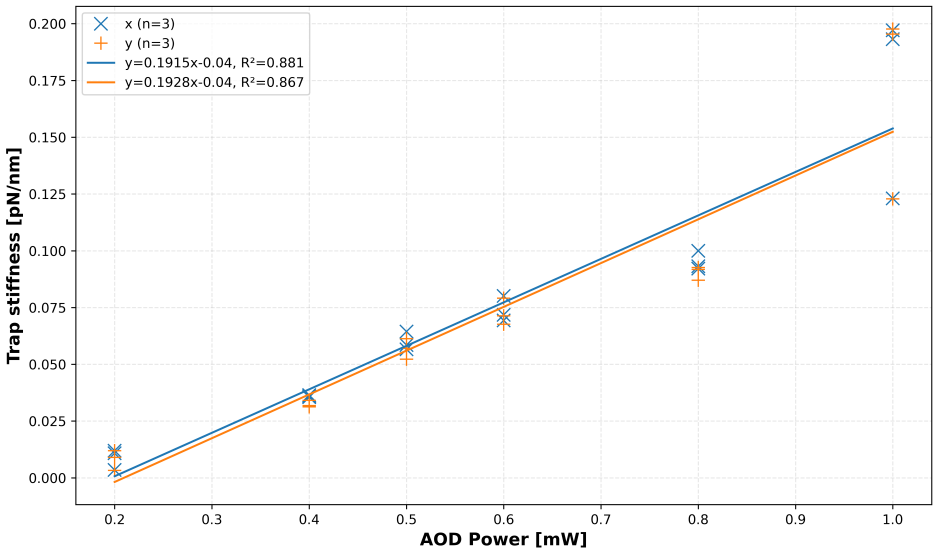

Figure 4.3: Trap stiffness as a function of AOD power.
Trap stiffness (pN nm^{-1}) as a function of AOD power (mW) X (blue) and Y (orange) direction. A linear fit to all data points (n = 4 measurements) is plotted.

4.2.3. Allan Variance Analysis

To determine the optimal data acquisition parameters for detection of translocation dynamics at elevated temperatures (~50°C), we performed AV analysis on bead position in our OT system. The loglog plot (Figure 4.4) shows two characteristic noise regimes. Our result does not show a characteristic three-regime behavior expected for optical tweezers measurements [61]. This is due to our restriciton of the x-domain on the AV plot to τ_{max} = 1 s. This restriction is chosen as we will not be not be downsampling our FtsH experimental data with τ > 1 s, because we need sufficient temporal resolution to distinguish individual translocation steps.

The AV reaches a minimum of σ^2_{min} = 0.158 nm^2 at τ_{opt} = 0.203 s for both lateral directions. This minimum represents the optimal observation window where thermal fluctuations are sufficiently averaged while low-frequency drift has not yet accumulated. The near-identical behavior in both lateral directions shows the isotropy of the optical trap and the absence of significant astigmatism. The low variability (standard error of mean $\pm$0.005 nm^2) across multiple measurements demonstrates reproducibility of trap performance.

Based on this analysis, we can select an averaging time for subsequent FtsH experiments. This choice represents a compromise between achieving sub-nanometer positional, sufficient for resolving nanometer scale translocation, and maintaining temporal resolution compatible with FtsH substrate threading dynamics. In chapter 5 we will discuss our informed decision based on relevant literature on AAA+ dynamics.

AV is determined independently (Figure 4.4), for both lateral trap directions (X and Y).

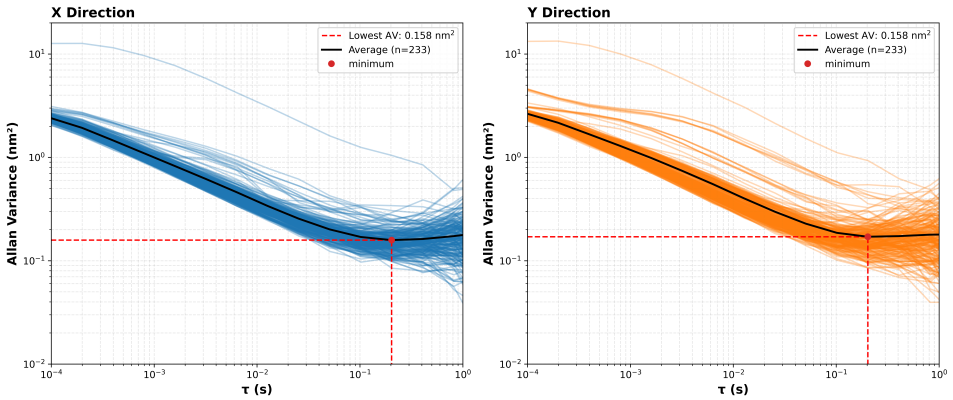

Figure 4.4: Allan variance analysis of our OT setup.
Pooled average (black) AV (σ_τ^2) versus averaging time τ for both lateral directions (X, blue; Y, orange), Data is pooled from 236 measurements across multiple days, recorded at ~50°C.

On average, our obtainable positional accuracy compares favorably with the differential back-focal-plane detection method reported by Nugent-Glandorf and Perkins, who achieved 0.1-nm resolution in 1 ms using a dual-laser differential detection system [62]. While their approach required two independent laser systems to subtract mechanical drift, our single-beam system achieves comparable precision (0.158 nm) through temporal averaging at a moderate sampling frequency (5 Hz, equivalent to 200 ms averaging time). This represents a practical trade-off: their method provides superior temporal resolution (1 kHz raw sampling) but requires substantially more complex instrumentation, whereas our approach sacrifices some temporal bandwidth to achieve sub-nanometer precision with a simpler optical configuration. Both approaches demonstrate that sub-nanometer position detection is achievable in optical trapping experiments when measurement noise is properly characterized and mitigated.

This comprehensive characterization of our optical trapping system establishes its suitability for single-molecule measurements of thermophilic FtsH protease dynamics. AOD calibration yielded spatial conversion factors with 0.5% relative uncertainty, enabling precise trap positioning across the sample plane. Trap stiffness measurements demonstrated that our system provides tunable trap stiffness spanning 0.02–0.20 pN nm^{-1}. AV analysis identified an optimal averaging time of 200 ms, yielding a position resolution of 0.158 nm, sufficient to resolve steps at the nanometer scale. Collectively, these validation measurements demonstrate that our instrument achieves sub-nanometer spatial precision at appropriate temporal resolution for characterizing AAA+ protease dynamics, providing a robust foundation for the single-molecule measurements presented in chapter 5.

5

Single-Molecule Optical Tweezers Measurements of AaFtsH-Mediated Substrate Translocation

5.1. Introduction

5.1.1. The Single-Molecule Vision: From Bulk Assays to Individual Events

The results from chapter 3 tell us that our purified detergent immobilized AaFtsH is active and can degrade its substrates. The calibration measurements presented in chapter 4 assure us that our instruments can measure bead position accurately and reliably. Yet, neither of these approaches directly addresses the mechanistic question central to this research: *what are the mechanical dynamics of AaFtsH as it unfolds, and translocates individual substrate molecules?*

We cannot answer these questions through bulk assays already reported on FtsH [13, 14, 63]. Thousands of interactions are reflected in an averaged snapshot: some proteases may be in initial contact with substrates, others may be mid-translocation, others may have just completed degradation. Single-molecule optical tweezers, should allow for direct observation of the trajectory of a single protease-substrate; mechanical interaction, unfolding, translocation, slipping, and release. Through direct position and force measurements, information about the fundamental functioning of the protease can be revealed. Where ensemble assays report rates and velocities, forces are central to protease function: the protease must generate sufficient force to denature its substrate to overcoming the free energy of the substrate's native fold. By directly measuring forces in individual interactions, OT provide a more detailed picture of the protease's mechanical behavior.

5.1.2. FtsH in the Context of AAA+ Protease Single-Molecule Studies

Single-molecule OT studies on AAA+ proteases have yielded remarkable insights. Starting in the early 2000s, pioneering studies by the Bustamante [27, 30, 64, 65], Fernandez [53, 54], and Baker [26, 28, 51, 52, 66, 67] groups applied optical tweezers to study AAA+ proteases, most notably ClpXP and Lon. These studies revealed that (summarised in Table 5.1):

ClpXP exhibits processive, ATP-dependent substrate translocation. When a ClpX hexamer engages a substrate with a terminal recognition motif, it pulls the substrate through a narrow central channel in the protease, unfolding structured domains en route to the ClpP catalytic chamber. Single-molecule measurements show that ATP hydrolysis is coupled to these steps: approximately one ATP is hydrolyzed per step, with a variable step size of 5–8 amino acids [26] or ~1–4 nm [28]. Remarkably, ClpXP can degrade multiple substrate domains processively. It can unfold and degrade titin I27 repeats one after another without releasing the substrate, which reflects that the energy released from ATP hydrolysis is partially retained to drive successive unfolding events [30, 31, 68].

ClpAP shows different mechanics from ClpXP. While ClpA is homologous to ClpX (both are distinct AAA+ helicases combining with proteases), ClpAP exhibits more less variable, slower translocation speeds and possibly different step sizes (lower variability variable and smaller steps of

~1–2 nm) than ClpXP [67]. Additionally, ClpA shows faster substrate unfolding [67] than ClpX, possibly due to increased grip strength from a double AAA+ ring [52]. This indicates that, despite sequence and structural similarities within the AAA+ family, individual members have evolved mechanistically distinct behaviors [10, 52].

Lon protease exhibits single-step, processive degradation. Unlike ClpXP, which processively translocates and cleaves multiple times, Lon appears to unfold substrates in a single rapid transition, and then release the unfolded product [51], maybe allowing multiple encounters with the same substrate. Additionally, Lon exhibits high processivity, completing substrate proteolysis of the entire substrate >90% once degradation is initiated [51]. This operational mode is mechanistically distinct from both ClpAP and ClpXP, further establishing the functional diversity within the AAA+ family. However, only a single publication reports the dynamics of Lon [51] exists thusfar, in contrast to the more extenisvely investigated ClpXP [30, 31, 68] and ClpAP [10, 52, 67] proteases.

Table 5.1: Comparison of kinetic and mechanochemical parameters for Lon, ClpAP, and ClpXP.
^{a} values are taken from ref [51], ^{b} values are taken from ref [67], ^{c} values are taken from ref [69], ^{d} values are taken from ref [28].

Parameter	Lon	ClpAP	ClpXP
Step size [nm]	1.66 ± 0.02^a	1.4 ± 0.5^b	1.3 ± 0.1^c
Translocation speed [nm s^{-1}]	3.4 ± 0.01^a	2.4 ± 0.1^c	3.4 ± 0.1^c
Step dwell time [s]	0.393 ± 0.002^a	0.4 ± 0.01^b	0.4^c
V13P degradation time [s]	$\sim 16^a$	$\sim 2^b$	$\sim 6^d$
V15P degradation time [s]	$\sim 27^a$	$\sim 6^b$	$\sim 17^d$
ATP hydrolysis [s^{-1}]	$\sim$ 2–2.5^a	$\sim 2.5^c$	$\sim 3.25^c$

These studies collectively establish that AAA+ proteases are mechanistically diverse: they differ in processivity, step size, force generation, and ATP coupling. This diversity likely reflects adaptation to different cellular niches and substrate types [3, 10]. Notably absent from this body of work is FtsH. While FtsH has been studied extensively via structural biology [18, 19, 43], and bulk biochemistry assays [11, 13, 14, 23, 44, 63], no single-molecule optical tweezers measurements of FtsH have been published thus far. This represents a significant gap and a clear opportunity for new mechanistic insights which we aim to fill.

5.1.3. Experimental Design: Tethering Strategy and Substrate Geometry

Our optical tweezers assay was designed to directly measure mechanical translocation by AaFtsH. The assay geometry is as follows:

Surface-bound AaFtsH: We immobilized full-length, membrane-integrated AaFtsH on the surface of a glass flow cell. This was achieved through a rigorous glass cleaning protocol, before coating the flow cell surface with streptavidin. The AaFtsH preparation (expressed in *E. coli* and purified as detailed in chapter 3) carries a biotin modification on its surface, allowing it to bind strongly and specifically to the streptavidin-coated glass surface. To reduce non-specific adsorption of other proteins and the silica bead (described below), we treated the entire surface with a blocking buffer containing BSA. The AaFtsH molecules, now immobilized on the surface, retain their catalytic activity (as we verified in chapter 3) while presenting their catalytic site toward the flow cell interior, positioned to engage substrates. Due to surface immobilisation of AaFtsH, autoproteolysis should not be an issue during OT experiments.

Substrate tethering between bead and surface-bound protease: We prepared a substrate consisting of titin I27-repeated domains bearing an ssrA degradation tag at the C-terminus (Figure 3.2). To tether this substrate between a trapped bead and a surface-bound AaFtsH, we employed a molecular linkers to the substrate: a DNA oligonucleotide bearing biotin at one end and a HaloTag at the other. The biotinylated end of the DNA linker was attached to a silica bead pre-coated with streptavidin purchased from vendors. The HaloTag-modified end of the DNA linker attaches to the substrate protein (the I27-ssrA construct, added via chemical conjugation). With this configuration, the substrate can now be tethered between the trapped bead (held by the optical trap) and the surface-bound AaFtsH.

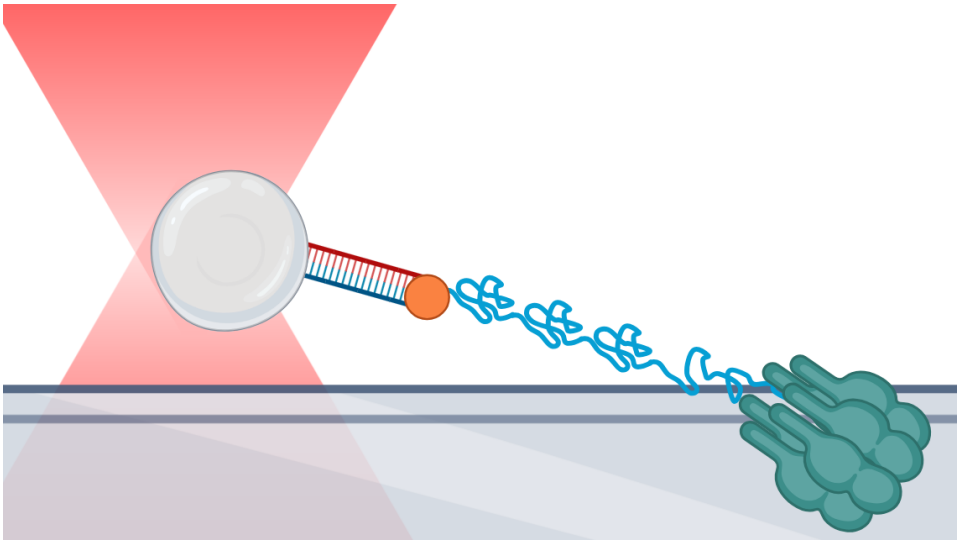

Figure 5.1: Schematic of optical tweezers assay for AaFtsH-mediated substrate degradation.
A silica bead (grey) is trapped by a focused infrared laser (red) and tethered to surface-immobilized AaFtsH protein (green) via a titin-I27$_4$ polyprotein substrate (blue). As AaFtsH processively unfolds and translocates the substrate, the bead is pulled out of the trap center, enabling real-time force and extension measurements.

Initiating substrate engagement: To tether the substrate between the bead and protease, we activated AaFtsH by heating the flow cell to >50°C and adding a buffer containing ATP (or in negative control experiments, ATP-γS). Force and position calibrations as described in chapter 4 are done for each bead. At this point, if AaFtsH engages the substrate and begins translocation, the protease will pull the substrate across the surface away from the trap center. By recording bead position with high temporal resolution (10 kHz sampling frequency), we directly measure changes in bead position relative to the trap center, which is our readout for substrate engagement and translocation.

The Tethering Verification Problem

We must address directly a challenge haunting all single-molecule optical tweezers studies of proteases: the difficulty in verifying that a measured signal actually corresponds to productive protease-substrate tethering.

The ideal single-molecule optical tweezers experiment measures one protein molecule interacting with one substrate molecule; the measured position change reflects the biochemistry of that single interaction. However, in practice, the flow cell contains many protease and substrate molecules. When a bead is brought close to the surface and force changes are observed, we must ask if this signal represents a productive interaction between the surface-bound protease and the substrate-tethered bead. Force changes can be due to non-specific adhesion between the bead and the surface as well.

In the most successful single-molecule protease studies (e.g., well-optimized ClpXP experiments), this ambiguity can be substantially reduced through experimental design and analysis: multiple independent observables can be measured (force, displacement, bead motion) that collectively distinguish productive interactions from artifacts. Furthermore, the reproducibility and consistency of measured signals across many trials (hundreds of repeated measurements) should provide statistical confidence that signals are real. There is no literature on reported success rates (the fraction of experimental trials yielding interpretable substrate translocation traces), we have learned that this is a technical challenge however.

Control experiments (assays without ATP, assays with ATP-γS) are designed to address this challenge. In the absence of ATP, AaFtsH should be inactive and should not translocate substrates; any signals in this condition likely represent non-specific adhesion. With ATP-γS (a non-hydrolyzable ATP analog), AaFtsH should bind ATP but not hydrolyze it; if signals appear only under conditions of ATP hydrolysis (native ATP) and not with ATP-γS, this would suggest that the signals are ATP-dependent and thus likely represent productive enzymatic engagement. However, we note that these controls are difficult to interpret definitively: the absence of signals in these conditions does not directly prove that signals are absent as reproducibility of tethering is hard, and the presence of signals with ATP-γS could reflect non-specific interactions.

Given these inherent challenges, we present our single-molecule measurements in this chapter with appropriate caution. We emphasize that our preliminary single-molecule observations, while representing the first such measurements of FtsH, should be viewed as foundational work establishing methodology rather than a true definitive characterization of FtsH mechanics. We will discuss which aspects of our data we regard as more robust and which aspects remain ambiguous or challenging to interpret.

5.1.4. Observable Mechanical Signals and Expected Observables

Our optical tweezers setup operated in a *position-clamp* mode, ensuring a constant trap position. The force on the bead is recorded as the force bead position changes. This contrasts with a *force-clamp* optical tweezers operation, where a constant force is applied and the displacement is measured. Position-clamp mode has the advantage of providing a stable reference frame and is well-suited to detecting discrete translocation events [33]. We measured the bead position relative to the trap center. Through trap stiffness calibration (subsection 2.2.4) for each individual bead, the force experienced by the bead can be accurately determined. In our experiments, we adjusted the AOD power to obtain trap stiffnesses spanning 0.01–0.2 pN nm^{-1}, appropriate for investigation of proteases [33].

We anticipate that successful interactions between substrate and AaFtsH would produce observable changes in the distance signal recorded during a position-clamp experiment (Figure 5.2). Literature suggests that FtsH is the evolutionairy closest relative to Lon [20], both a self-contained AAA+ protease with high structural and sequential similarity [9]. Based on the results summarised in Table 5.1, we expect the following observables:

- **Translocation events:** Following unfolding, AaFtsH should translocate the unfolded substrate through its catalytic channel, showing characteristic kinetics. Based on the published on AAA+ proteases summarised in Table 5.1, we expect AaFtsH to translocate the substrate with discrete steps of ~1–2nm with low variability, similar to Lon.
- **Mechanical unfolding transitions:** Discrete jumps in bead position corresponding to the unfolding of the titin I27 domains. Each I27 domain has a characteristic elongation distance when unfolded. This can occur directly, or via an intermediate state [50, 52, 70], characterised via three states; folded (*F*), intermediate (*I*), and unfolded (*U*). We expected to observe stepwise increases in extension as domains are unfolded comparable contour length increases between folding states summarised in Table 5.2. Additionally, we expect to see HaloTag unfolding characterised by a single ~66 nm jump [71].
- **Processivity patterns:** We anticipate that successive titin domains are translocated with lower processivity compared to Lon. While Lon demonstrates high processivity [51], and possibly higher degradation rates than our detergent-immobilized AaFtsH (Figure 3.3), FtsH reportedly lacks robust unfoldase activity [25]. Additionally, research suggests that FtsH degradation is highly sensitive to substrate thermostability [14, 20]. Given the thermostability of titin, we hypothesize that our AaFtsH may struggle to degrade multiple titin domains continuously. V13P and V15P titin variants, with unique thermostabilities them ideal substrate to rigorously test the limits of AaFtsH processivity and the influence of substrate stability.

Our passive position-clamp configuration yields a characteristic force-ramping periodic profile. As the motor pulls the substrate, tension rises until it reaches the critical unfolding force of a domain (5.2). Ideally, for a homopolymeric substrate like titin-$I27_4$, these rupture events should occur at comparable forces, creating a series of peaks roughly aligned along the Y-axis. However, due to the stochastic nature of unfolding, these peaks distribute around a mean characteristic stability limit. This contrasts widely applied dual-trap force clamp experiments [28, 30, 52, 67, 68]. In such setups, the tension on the substrate is held constant by a feedback loop, removing a position-based force limit at which the substrate unfolds.

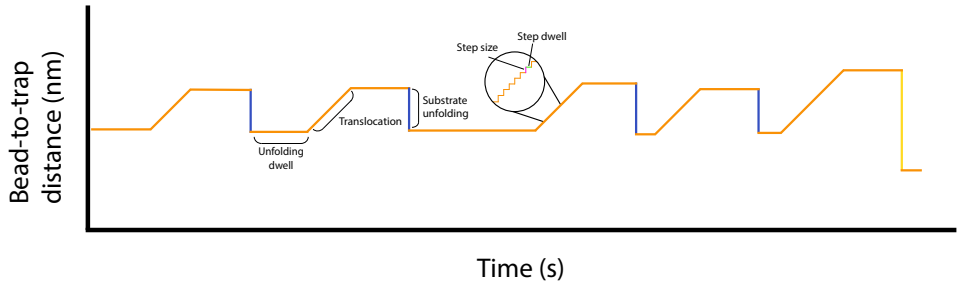

Figure 5.2: Schematic of ecpected single-molecule traces for degradation of a multi-domain substrate. The schematic plot shows the relative bead distance between bead and trap center plotted against time. As AaFtsH interacts with the substrate, the bead is pulled away from the trap center. Substrate unfolding will result in a sharp decrease in relative distance. Unfolding dwell and translocation by AaFtsH is indicated with accolades. Individual translocation steps (pink) and dwell (green) are shown in an enlarged view with. Titin-I27 unfolding events are indicated in blue, HaloTag unfolding event is indicated in yellow. The different Y-axis unfolding limit reflects the higher force needed to unfold the HaloTag.

Table 5.2: Overview of the contour length increase between different titin folding states. Contour length increases (nm) of different titin variants are given for changes in folding state; folded (*F*), intermediate (*I*), and unfolded (*U*). Data acquired from [52]

Titin variant	$F \rightarrow I$	$I \rightarrow U$	$F \rightarrow U$
V13P	11.2 ± 0.3	19.4 ± 0.4	28.6 ± 0.6
V15P	13.1 ± 0.3	23.2 ± 0.4	30.6 ± 0.7

Finding Steps in Noisy Signals

Single-molecule optical tweezers experiments generate time-dependent measurements of molecular motion at unprecedented spatial and temporal resolution, yet these measurements inherently contain substantial experimental noise that obscures the underlying discrete molecular events. This challenge has driven the development of increasingly sophisticated analytical approaches, each with different assumptions about the nature of the noise, the structure of the underlying signal, and the computational strategies most appropriate for signal recovery [72, 73].

The χ-square method [74] is most cited within single molecule research, in part to its intuitivity and simple implementation [72, 73]. Despite these advances, a few key weaknesses are present [73, 75]; (1) The method is not guaranteed to find a global optimum, (2) the performance of this method depends heavily on user-selected paramters. Therefore, we opted for the KV (Kalafut-Visscher) method, an objective, model-independent [76] method for step-fitting.

The heart of the KV method is the application of the SIC (Schwarz Information Criterion, Equation 5.1). The SIC is computed based on all the supplied data and ranks step-detection models [76]. For different candidate models, each specifying a particular number of steps at unique locations, the likelihood is computed. The SIC combines the maximum likelihood with a penalty term (increasing with the number of parameters), meant to balance model complexity. This method possesses several strengths; (1) Users do not need to specify the number of steps to detect or any statistical thresholds [76], (2) the model demosntrates superior performance at high noise levels [72, 73, 76]. Despit these strengths, we must acknowledge some limitations to the KV method; (1) the method is computationally more intensive compare to other step-finding methods [72, 73], (2) the method still assumes Gaussian, independent noise eventhough optical tweezers setups have correlated noise sources [75].

$$SIC = \underbrace{-2\log(\mathcal{L}(\theta))}_{\text{Likelihood term}} + \underbrace{p\log(n)}_{\text{Penalty term}} \tag{5.1}$$

5.1.5. Allan Variance-Optimized Step Detection

Optical tweezers data exhibits complex noise characteristics that violate the Gaussian white noise (GWN) assumption underlying (KV) and Kerssemakers method [74, 76]. At high frequencies, viscous damping colours the noise spectrum. At low frequencies, instrumental drift or local convection

streams introduce non-stationary fluctuations [75]. When applied to such coloured noise, the KV algorithm can misidentify correlated fluctuations as rapid translocation substeps, leading to noise overfitting and spurious step detection [75]. To address this limitation, we propose a dual-stage optimization protocol that combines AV analysis with KV step fitting (AVKV method).

The novel AVKV method proceeds as follows: first, we acquire high-bandwidth position data (10 MHz) from trapped beads under experimental conditions. Next, the temporal domain dominated by GWN is identified (-1 on the AV plot). Within this GWN regime, the averaging window offering the highest spatial resolution τ_{GWN}. The τ_{GWN} is applied to raw data resampling. This AV-based downsampling ensures us our data complies to the GWN assumption of the KV method, which now operates within its valid statistical framework.

To validate the AVKV method, we performed synthetic step trajectories obscured by realistic noise models. Unlike earlier KV validation, which tested performance only against Gaussian white noise [72, 76], we systematically evaluated step detection with simulated data obscured with mixed white and pink noise sources, depicting SM-OT noise profiles more accurately. For each noise model, we compared naive KV step fitting (applied to a standard resampling frequency of 300 Hz) against AV-based KV fitting. The result of our system AV analysis (subsection 4.2.3) shows highest spatial resolution at τ = 0.2 ms. Average dwell times of similar AAA+ proteases (Table 5.1) are ~400 ms. To prevent the risk of Nyquist-like undersampling for step detection, we set a lower limit on the averaging window. We chose five times the characteristic turnover rate of similar proteases (5×0.4 s^{-1}). This ensures that the sampling window remains sufficiently narrow to resolve the stochastic dwell times expected for the FtsH hydrolysis cycle.

We provide the AVKV implementation as open-source Python code [77], addressing limitations of the original LabVIEW and C implementations [76] that either require expensive commercial licenses or advanced programming expertise. Our implementation includes: (1) automated AV computation and optimal bandwidth selection, (2) adaptive AV-based downsampling of experimental data, (3) KV step fitting, and (4) visualization tools. This workflow establishes a transparent, reproducible framework for single-molecule optical tweezers data analysis, directly addressing the unjustified choice of arbitrary resampling frequencies in the AAA+ literature. The accessible toolkit enables researchers to quantitatively report their optical tweezers system accuracy using standardized AV metrics, promoting reproducibility and comparative analysis across laboratories, a gap in current single-molecule literature where justification of resampling choices are often neglected [26, 27, 30, 52].

5.2. Results and Discussion

Next, we present the validation of our AVKV method and its application to our SM-OT measurements. We interpret them in light of the challenges and opportunities common to this technique. This section presents representative single-molecule traces, statistics on events, and the outcomes of control experiments. The interpretation of these results are discussed, reflecting critically on what can be confidently concluded and what remains ambiguous. We emphasize that, while our work does not yield the clear, high-resolution periodic unfolding records obtained in canonical studies of other AAA+ proteases [27, 28, 30, 51, 52, 64, 67, 68], it represents progress on a mechanistically important but previously unstudied protease and establishes methodological foundations for future single-molecule studies of FtsH and other (thermophilic) proteases.

5.2.1. AVKV Method Validation

Comparitive analysis of step-fitting performance on simulated datasets (n=10) reveals that the AVKV method (Figure 5.3a) significantly outperforms the naive KV method (Figure 5.3b). The performance of both methods was determined based on step detection sensitivity (se, $\frac{\text{correct matches}}{\text{total true steps}}$) and precision (pr, $\frac{\text{correct matches}}{\text{total detected steps}}$).

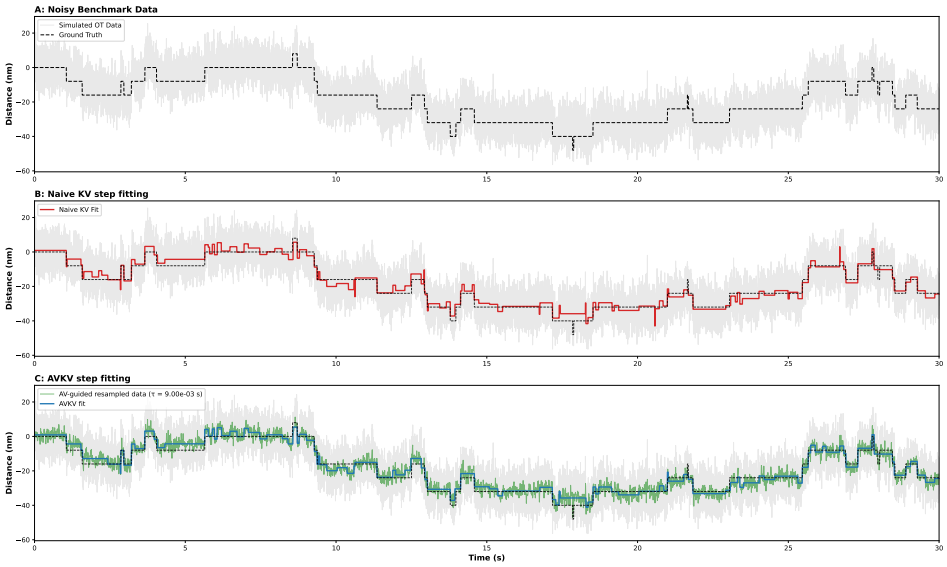

Figure 5.3: Comparison between naive and AVKV step fitting methods.
A | Ground truth signal (striped) generated as described in [76], with the additional noise sources. **B** | Naive KV step fitting to data to $f = 300$ Hz. **c** | AVKV stepfitting.

While both algorithms demonstrated a similar sensitivity, identifying approximately half of the ground truth steps (Naive KV se = 0.506 $\pm$ 0.054; AVKV se = 0.504 $\pm$ 0.054), they differed markedly in their precision. The naive KV method yielded a lower precision (pr = 0.350 $\pm$ 0.042), indicating that a substantial portion of detected *steps* are due to overfitting of noise. In contrast, the AVKV method achieved a ~20% increase in precision (pr = 0.415 $\pm$ 0.032).

This improvement indicates that the Allan Variance-guided resampling effectively suppresses false positives without compromising the detection of real events. Crucially, the similarity in sensitivity scores confirms that the resampling process did not average out fast events. This validation confirms that we can confidently apply our novel AVKV-method to noisy SM-OT data, containing varying noise sources.

5.2.2. AaFtsH OT experiments

Experiments with Titin-V13P as a substrate

At the experimental temperature of ~50°C, we observed transient changes in bead-to-trap distance during FtsH-substrate tethering experiments (Figure 5.4). However, unlike mechanically stable substrates such as titin I27 at room temperature [54], the expected, periodic unfolding pattern (Figure 5.1), characteristic of sequential domain unfolding was absent from our measurements. The traces shown in Figure 5.4a-c indicate substrate interactions with AaFtsH after scanning the surface. Measurements show that something keeps the bead out of the trap center, quickly falling back in discrete steps, close to titin^{V13P} or HaloTag unfolding (Table 5.2). However, due to the absence of multiple such events during a single measurement, and low reproducability of representative (~10 traces from 344 measurements) traces, we are cautious.

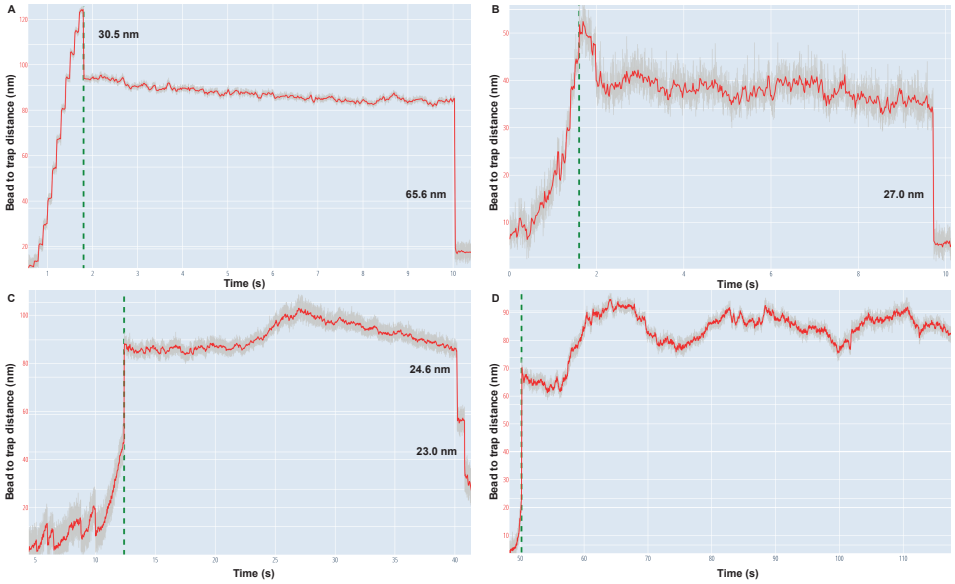

Figure 5.4: Representative traces of initial susbtrate engagement by AaFtsH.
All subfigures show the raw data (gray) and the AV-based downsampled (red) bead position trace. The bead is scanned across the surface to initiate susbtrate tethering, when position signal changes, a measurement is initiated (green dotted line). **a**-**b** | zoomed in trace to show signal change when substrate engagement is initiated during surface scanning with the piezo stage. **c**-**d** | traces showing transient bead position changes.

To validate the physiological relevance of our measurements, we applied the AVKV step-fitting method to extract the kinetic fingerprint of the observed translocation events. By comparing the statistical distribution of step sizes and dwell times to established literature, we assessed whether these traces represent genuine AaFtsH activity.

The analyzed traces (Figure 5.4) reveal distinct stepwise increases in bead-to-trap distance, consistent with the translocation behavior reported for the homologous AAA+ protease Lon in similar single-trap optical tweezers experiments [51]. However, a standard processive model does not fully capture the dynamics observed. As shown in Figure 5.4c, AaFtsH frequently exhibits slipping, characterized by sequences of rapid backward steps. FtsH's processivity appears sensitive to mechanical load. Increased bead-to-trap displacements show increased slipping. Since the restoring force of the optical trap increases linearly with displacement, these data indicate that FtsH is prone to backsliding when working against higher opposing forces. This force-dependent substrate interaction may reflect the unique ceullar nich of FtsH. The motor implies a mechanical sensing mechanism, where it releases or slips the substrate when the force required to unfold a stable domain exceeds the motor's power output.

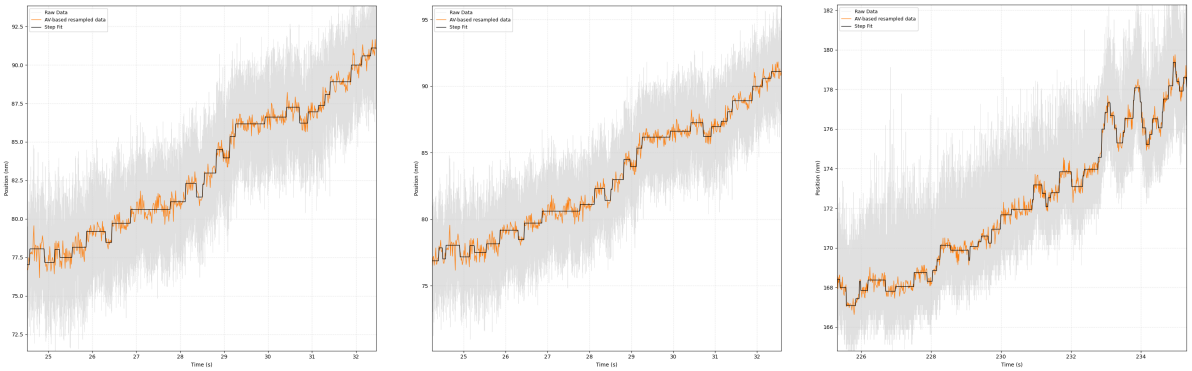

Figure 5.5: Representative stepping in AaFtsH translocation trajectories.
Raw data (gray) was resampled through and fitted with the AVKV method, using different averaging windows τ_{GWN} for individual traces.

Independent results from step-fitting for three independent measurements are pooled and analysed (Figure 5.6-Figure 5.8). This analysis shows that the mean step size during AaFtsH translocation is 1.146 $\pm$ 0.643 nm, with a mean step dwell of 0.294 $\pm$ 0.283 s Figure 5.6. The notable variance in these distributions is characterstic of SM experiments at elevated temperatures, where brownian motion broadens the distribution. The histograms show exponential and gaussian characteristics, respectively. These results compare with step sizes and dwell times of ClAP, ClpXP, and Lon proteases (Table 5.1), confirming that these analysed measurements are representative of AaFtsH substrate translocation.

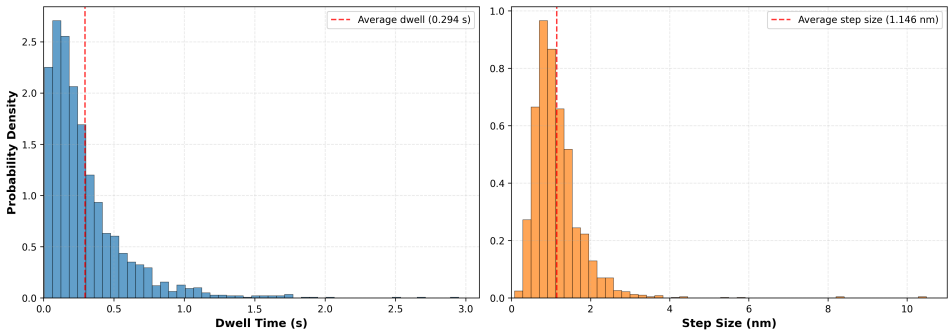

Figure 5.6: Histogram of AaFtsH dynamical parameters.
Distribution of AaFtsH step dwell times (**a**), and step sizes (**b**) during titin-V13P translocation. A mean step dwell of 0.294 $\pm$ 0.283 s, and a step size of 1.146 $\pm$ 0.643 nm was recorded.

To mitigate binning artifacts inherent to histograms, we analyzed the Cumulative Distribution Functions (CDFs) of these parameters (Figure 5.7). The step size distribution complies well to a Gaussian model, confirming that the variation in step length is due to thermal noise on the bead rather than variable motor geometry. Meanwhile, the dwell time distribution (Figure 5.7a) provides insight into the rate-limiting steps of the reaction. The fit assumes a single exponential distribution, indicating a single rate-limiting event within the hydrolysis cycle.

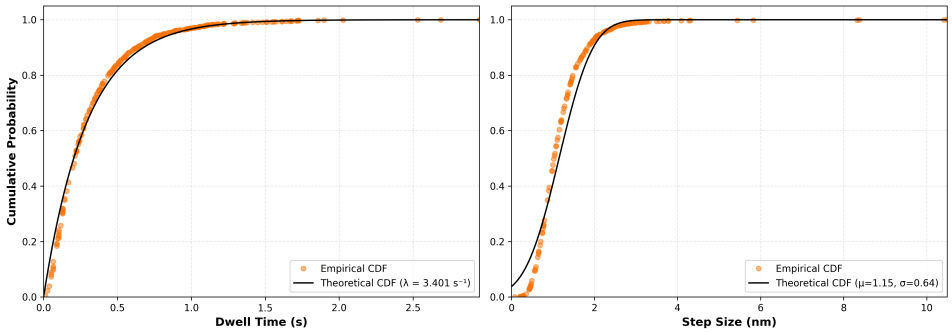

Figure 5.7: Cumulative distribution of AaFtsH physical parameters.
Cumulative distribution functions of step dwell times (**a**), and step sizes (**b**) with theoretical fits.

Finally, we investigated potential coupling between the spatial and temporal domains of the motor. As shown in Figure 5.8, there is no significant correlation between the duration of a dwell and the size of the subsequent step. This lack of correlation suggests that the mechanical step size is a robust structural feature of the FtsH protease (as proposed by [78]), independent of the stochastic waiting times imposed by ATP hydrolysis kinetics.

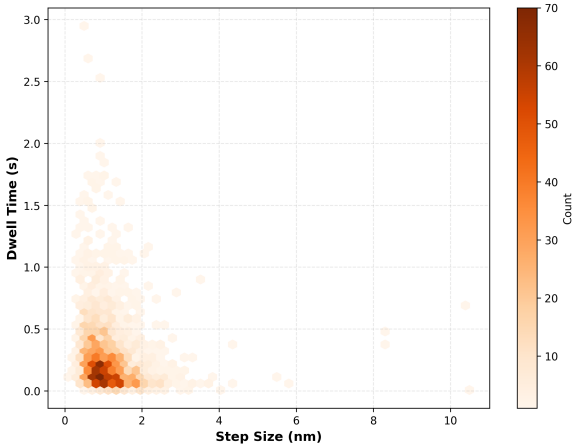

Figure 5.8: Correlation between step size and step dwell.
Scatter plot of step-dwell plotted against step size.

5.2.3. Titin thermal destabilization

A distinguishing feature of these measurements was the absence of the characteristic periodic unfolding pattern typically observed for titin-I27 substrates in single-molecule experiments. While comparable statistics on step sizes are recorded after substrate engagement, we successfully recorded substrate translocation, the expected unfolding events were not detected.

We hypothesize that this is a consequence of the experimental temperature (50°C) combined with the destabilizing V13P mutation. While wild-type titin-I27 is mechanically robust at room temperature, previous studies indicate its stability is highly temperature-dependent. The force required to unfold titin decreases significantly as temperature rises, consequently increasing the unfolding rate[79, 80]. Furthermore, the V13P mutation is known to disrupt the hydrogen bonding network critical for the domain's mechanical resistance [53]. Therefore, it might be the case that at 50°C, the titin V13P substrate exists in a thermally destabilized or state. Consequently, observed measurements reflect AaFtsH translocation of a largely unfolded polypeptide chain rather than forcibly unraveling of a structured domain. We propose that the use of titin V15P as a substrate might mitigate these effects, allowing us to resolve the expected periodic unfolding pattern.

5.2.4. Limitations in Experimental Geometry

Finally, the quantitative interpretation of our step size must consider the geometric constraints of the surface-coupled optical tweezers assay. The step size is derived from the lateral-displacement of the bead; however, the actual contour length change of the DNA-protein tether depends on the angle of the tether relative to the surface.

Given a bead diameter of 1 μm and a DNA handle length of similar scale (~3500 bp=~1 μm), any lateral offset between the bead center and the anchoring point creates a tether angle θ. The measured step is therefore a projection of the actual translocation step size, described by. Variations in the specific attachment point of the substrate on the bead surface introduce uncertainty in this angle. Consequently, our reported step size of 1.15 nm represents a lower bound of the true translocation distance. Despite these geometric and thermal broadening effects, the detection of distinct, periodic steps at 50°C provides strong evidence for the, mechanochemical nature of AaFtsH.

6

Conclusions & Outlook

6.1. Conclusions

This thesis presents a comprehensive single-molecule characterization of the thermophilic AAA+ protease AaFtsH. By bridging biochemical bulk assays with advanced OT signal processing, we established a rigorous methodology to investigate the nanodynamics of a membrane-bound motor at elevated temperatures.

Biochemical Validation

First, we validated the biological integrity of detergent-solubilized AaFtsH. Our degradation assays confirmed that the protease retains proteolytic activity against both unstructured (β-casein) and structured (titin-I27 variants) substrates across a physiological temperature range (56–74°C). Crucially, we demonstrated that AaFtsH maintains catalytic functionality at 50°C, the operational limit of our optical trapping system. This validation provides the necessary biochemical prerequisite for force spectroscopy measurements.

Methodological Innovation: The AVKV method

A central challenge of this work was resolving sub-nanometer motor steps within the high thermal noise environment of single-molecule interactions at 50°C. Standard step-finding algorithms, such as the Kalafut-Visscher (KV) method, rely on the assumption that experimental noise follows a Gaussian White Noise distribution[74, 76]. However, our system analysis confirmed that OT data exhibits more complex noise characteristics. To address this, we developed and validated the Allan Variance-based Kalafut-Visscher method. This dual-stage protocol uses Allan Variance analysis to identify the temporal regime where the system noise is distinctly Gaussian. By downsampling raw data to this optimal integration time, we ensure compliance with the statistical assumptions of the KV step-fitter. To validate this approach, we tested the method against synthetic step trajectories obscured by realistic mixed (white and pink) noise models, demonstrating that AVKV significantly outperforms naive KV fitting in low signal-to-noise conditions representative for single molecule optical tweezers experiments. Furthermore, to democratize this analysis, we implemented the AVKV method as an open-source Python toolkit [77], providing the field with a transparent, reproducible framework for data resampling that replaces arbitrary frequency selection with standardized AV metrics.

Kinetic Characterization

Applying the AVKV method to our AaFtsH traces provided the first single-molecule evidence of discrete translocation steps by this protease. We resolved a mean step size of 1.15$\pm$0.6 nm and a dwell time of 0.29±0.3 s. The lack of correlation between dwell time and step size indicates that the mechanical stroke is a robust structural feature, uncoupled from the stochasticity of ATP hydrolysis.

Limitations

These findings must be interpreted within specific experimental constraints. The information gathered from AaFtsH OT experiments sends mixed signals. We observed step sizes comparable to other

AAA+ proteases. Measurements indicated individual substrate unfolding steps. However, we did not observe the characteristic periodic unfolding patterns of the titin-V13P substrate. We hypothesize that the combination of the V13P destabilizing mutation and the 50°C experimental temperature renders the substrate thermally unstable. Additionally, the surface-coupled geometry introduces a cosine error due to the tether angle; thus, our reported step size of 1.15 nm represents a lower bound of the true translocation distance. Despite these limitations, the detection of periodic, ATP-dependent steps establishes the first records of the mechanochemical nature of AaFtsH.

6.2. Future Directions

The methodology and findings presented here open several avenues for advancing the understanding of FtsH and other thermophilic motors.

Standardization of Single-Molecule Data Analysis Beyond the specific characterization of AaFtsH, this thesis addresses a systematic issue within the single-molecule community: the lack of standardized metrics for determining instrumental precision. Currently, many optical tweezers studies report step sizes based on arbitrary resampling frequencies without justifying how these bandwidths relate to their noise floors [26, 27, 30, 52]. This arbitrary data processing obscures the line between genuine kinetic events and noise artifacts. By releasing our AVKV implementation as an open-source Python toolkit, we aim to solve this problem. We propose that future single-molecule studies adopt Allan Variance analysis as a mandatory quality control step. Adoption of this standardized, transparent workflow will ensure that reported motor steps reflect the biological reality of the enzyme rather than undocumented manual tuning of the analysis parameters

The most immediate priority for future experimentation is the stabilization of the substrate. Future assays should utilize the wild-type titin-I27 domain or the more stable titin-V15P variant, which may retain sufficient fold stability at elevated temperatures to permit the observation of sequential, force-induced unfolding. Alternatively, investigating non-thermophilic FtsH variants at room temperature could bypass thermal instability issues, though this would sacrifice unique insights gained from studying the robust Aquifex variant.

From a technical perspective, overcoming the geometric limitations of surface-coupled assays is essential. Transitioning to a dual-trap assay would eliminate the tether angle uncertainty (cosine error) inherent to surface experiments. By suspending the FtsH-substrate complex between two trapped beads, the translocation vector would align perfectly with the measurement axis, providing a more accurate determination of the absolute step size.

Finally, expanding this research to include the membrane environment would provide the most physiological context. AaFtsH is a membrane-anchored protease, and its extraction into detergent micelles may alter inter-subunit coordination. Future studies could employ nanodiscs or liposomes to reconstitute AaFtsH in distinct lipid bilayers. Investigating how membrane composition, fluidity, and lateral tension influence the pulling power and processivity of FtsH would bridge the gap between single-molecule biophysics and cellular membrane biology, shedding light on how this essential protease maintains proteostasis in the chaotic environment of the cell membrane.

Bibliography

[1] Melisa Merdanovic et al. “Protein Quality Control in the Bacterial Periplasm”. In: *Annual Review of Microbiology* 65.1 (Oct. 13, 2011), pp. 149–168. DOI: 10.1146/annurev-micro-090110-102925.

[2] Sanjay B. Hari and Robert T. Sauer. “The AAA+ FtsH Protease Degrades an ssrA-Tagged Model Protein in the Inner Membrane of *Escherichia Coli*”. In: *Biochemistry* 55.40 (Oct. 11, 2016), pp. 5649–5652. DOI: 10.1021/acs.biochem.6b00920.

[3] Phyllis I. Hanson and Sidney W. Whiteheart. “AAA+ Proteins: Have Engine, Will Work”. In: *Nature Reviews Molecular Cell Biology* 6.7 (July 2005), pp. 519–529. DOI: 10.1038/nrm1684.

[4] Lakshminarayan M Iyer et al. “Evolutionary History and Higher Order Classification of AAA+ ATPases”. In: *Journal of Structural Biology* 146.1–2 (Apr. 2004), pp. 11–31. DOI: 10.1016/j.jsb.2003.10.010.

[5] Paul A Tucker and László Sallai. “The AAA+ Superfamily—a Myriad of Motions”. In: *Current Opinion in Structural Biology* 17.6 (Dec. 2007), pp. 641–652. DOI: 10.1016/j.sbi.2007.09.012.

[6] Vanessa Carvalho et al. “The Cytoplasmic Domain of the AAA+ Protease FtsH Is Tilted with Respect to the Membrane to Facilitate Substrate Entry”. In: *Journal of Biological Chemistry* 296 (Jan. 2021), p. 100029. DOI: 10.1074/jbc.RA120.014739.

[7] Ramona E. Duman and Jan Löwe. “Crystal Structures of Bacillus Subtilis Lon Protease”. In: *Journal of Molecular Biology* 401.4 (Aug. 2010), pp. 653–670. DOI: 10.1016/j.jmb.2010.06.030.

[8] Tania A. Baker and Robert T. Sauer. “ATP-dependent Proteases of Bacteria: Recognition Logic and Operating Principles”. In: *Trends in Biochemical Sciences* 31.12 (Dec. 2006), pp. 647–653. DOI: 10.1016/j.tibs.2006.10.006.

[9] Rya Ero et al. “Structural Insights into the Membrane-Bound Proteolytic Machinery of Bacterial Protein Quality Control”. In: *Biochemical Society Transactions* 52.5 (Oct. 30, 2024), pp. 2077–2086. DOI: 10.1042/BST20231250.

[10] Adrian O. Olivares, Tania A. Baker, and Robert T. Sauer. “Mechanistic Insights into Bacterial AAA+ Proteases and Protein-Remodelling Machines”. In: *Nature Reviews Microbiology* 14.1 (Jan. 2016), pp. 33–44. DOI: 10.1038/nrmicro.2015.4.

[11] Qian Chai et al. “The ssrA-Tag Facilitated Degradation of an Integral Membrane Protein”. In: *Biochemistry* 55.16 (Apr. 26, 2016), pp. 2301–2304. DOI: 10.1021/acs.biochem.6b00038.

[12] Julia M. Flynn et al. “Overlapping Recognition Determinants within the ssrA Degradation Tag Allow Modulation of Proteolysis”. In: *Proceedings of the National Academy of Sciences* 98.19 (Sept. 11, 2001), pp. 10584–10589. DOI: 10.1073/pnas.191375298.

[13] Sanjay B. Hari et al. “FtsH Degrades Kinetically Stable Dimers of Cyclopropane Fatty Acid Synthase via an Internal Degron”. In: *Molecular Microbiology* 119.1 (Jan. 2023), pp. 101–111. doi: 10.1111/mmi.15009.

[14] Juhee P. Morehouse, Tania A. Baker, and Robert T. Sauer. “FtsH Degrades Dihydrofolate Reductase by Recognizing a Partially Folded Species”. In: *Protein Science* 31.9 (Sept. 2022), e4410. doi: 10.1002/pro.4410.

[15] Yousuf A. Khan, K. Ian White, and Axel T. Brunger. “The AAA+ Superfamily: A Review of the Structural and Mechanistic Principles of These Molecular Machines”. In: *Critical Reviews in Biochemistry and Molecular Biology* 57.2 (Mar. 4, 2022), pp. 156–187. doi: 10.1080/10409238.2021.1979460.

[16] JiaBei Lin, James Shorter, and Aaron L. Lucius. “AAA+ Proteins: One Motor, Multiple Ways to Work”. In: *Biochemical Society Transactions* 50.2 (Apr. 29, 2022), pp. 895–906. doi: 10.1042/BST20200350.

[17] Szymon Krzywda et al. “The Crystal Structure of the AAA Domain of the ATP-Dependent Protease FtsH of Escherichia Coli at 1.5 Å Resolution”. In: *Structure* 10.8 (Aug. 2002), pp. 1073–1083. doi: 10.1016/S0969-2126(02)00806-7.

[18] Hajime Niwa et al. “Hexameric Ring Structure of the ATPase Domain of the Membrane-Integrated Metalloprotease FtsH from Thermus Thermophilus HB8”. In: *Structure* 10.10 (Oct. 2002), pp. 1415–1424. doi: 10.1016/S0969-2126(02)00855-9.

[19] Marina Vostrukhina et al. “The Structure of *Aquifex Aeolicus* FtsH in the ADP-bound State Reveals a C_2 -Symmetric Hexamer”. In: *Acta Crystallographica Section D Biological Crystallography* 71.6 (June 1, 2015), pp. 1307–1318. doi: 10.1107/S1399004715005945.

[20] Lanbo Yi et al. “Recent Advances in Understanding the Structural and Functional Evolution of FtsH Proteases”. In: *Frontiers in Plant Science* 13 (Apr. 6, 2022), p. 837528. doi: 10.3389/fpls.2022.837528.

[21] Prakash Koodathingal et al. “ATP-dependent Proteases Differ Substantially in Their Ability to Unfold Globular Proteins”. In: *Journal of Biological Chemistry* 284.28 (July 2009), pp. 18674–18684. doi: 10.1074/jbc.M900783200.

[22] Samar A. Mahmoud, Berent Aldikacti, and Peter Chien. “ATP Hydrolysis Tunes Specificity of a AAA+ Protease”. In: *Cell Reports* 40.12 (Sept. 2022), p. 111405. doi: 10.1016/j.celrep.2022.111405.

[23] Shinobu Chiba, Yoshinori Akiyama, and Koreaki Ito. “Membrane Protein Degradation by FtsH Can Be Initiated from Either End”. In: *Journal of Bacteriology* 184.17 (Sept. 2002), pp. 4775–4782. doi: 10.1128/JB.184.17.4775-4782.2002.

[24] Shinobu Chiba et al. “Length Recognition at the N-terminal Tail for the Initiation of FtsH-mediated Proteolysis”. In: *EMBO reports* 1.1 (July 2000), pp. 47–52. doi: 10.1093/embo-reports/kvd005.

[25] Christophe Herman et al. “Lack of a Robust Unfoldase Activity Confers a Unique Level of Substrate Specificity to the Universal AAA Protease FtsH”. In: *Molecular Cell* 11.3 (Mar. 2003), pp. 659–669. doi: 10.1016/S1097-2765(03)00068-6.

[26] Marie-Eve Aubin-Tam et al. “Single-Molecule Protein Unfolding and Translocation by an ATP-Fueled Proteolytic Machine”. In: *Cell* 145.2 (Apr. 2011), pp. 257–267. doi: 10.1016/j.cell.2011.03.036.

[27] Rodrigo A. Maillard et al. “ClpX(P) Generates Mechanical Force to Unfold and Translocate Its Protein Substrates”. In: *Cell* 145.3 (Apr. 2011), pp. 459–469. doi: 10.1016/j.cell.2011.04.010.

[28] Juan Carlos Cordova et al. “Stochastic but Highly Coordinated Protein Unfolding and Translocation by the ClpXP Proteolytic Machine”. In: *Cell* 158.3 (July 2014), pp. 647–658. doi: 10.1016/j.cell.2014.05.043.

[29] Matthias Uthoff and Ulrich Baumann. “Conformational Flexibility of Pore Loop-1 Gives Insights into Substrate Translocation by the AAA+ Protease FtsH”. In: *Journal of Structural Biology* 204.2 (Nov. 2018), pp. 199–206. doi: 10.1016/j.jsb.2018.08.009.

[30] Maya Sen et al. “The ClpXP Protease Unfolds Substrates Using a Constant Rate of Pulling but Different Gears”. In: *Cell* 155.3 (Oct. 2013), pp. 636–646. doi: 10.1016/j.cell.2013.09.022.

[31] Ohad Iosefson et al. “Dissection of Axial-Pore Loop Function during Unfolding and Translocation by a AAA+ Proteolytic Machine”. In: *Cell Reports* 12.6 (Aug. 2015), pp. 1032–1041. doi: 10.1016/j.celrep.2015.07.007.

[32] Steven B. Smith, Yujia Cui, and Carlos Bustamante. “Optical-Trap Force Transducer That Operates by Direct Measurement of Light Momentum”. In: *Methods in Enzymology*. Vol. 361. Elsevier, 2003, pp. 134–162. isbn: 978-0-12-182264-4. doi: 10.1016/S0076-6879(03)61009-8.

[33] Carlos J. Bustamante et al. “Optical Tweezers in Single-Molecule Biophysics”. In: *Nature Reviews Methods Primers* 1.1 (Mar. 25, 2021), p. 25. doi: 10.1038/s43586-021-00021-6.

[34] Keir C. Neuman and Steven M. Block. “Optical Trapping”. In: *Review of Scientific Instruments* 75.9 (Sept. 1, 2004), pp. 2787–2809. doi: 10.1063/1.1785844.

[35] Alexander Rohrbach and Ernst H. K. Stelzer. “Optical Trapping of Dielectric Particles in Arbitrary Fields”. In: *Journal of the Optical Society of America A* 18.4 (Apr. 1, 2001), p. 839. doi: 10.1364/JOSAA.18.000839.

[36] Hu Zhang and Kuo-Kang Liu. “Optical Tweezers for Single Cells”. In: *Journal of The Royal Society Interface* 5.24 (July 6, 2008), pp. 671–690. doi: 10.1098/rsif.2008.0052.

[37] Keir C Neuman and Attila Nagy. “Single-Molecule Force Spectroscopy: Optical Tweezers, Magnetic Tweezers and Atomic Force Microscopy”. In: *Nature Methods* 5.6 (June 2008), pp. 491–505. doi: 10.1038/nmeth.1218.

[38] Soham Mukherjee et al. “Single-Molecule Optical Tweezers As a Tool for Delineating the Mechanisms of Protein-Processing Mechanoenzymes”. In: *ACS Omega* 8.1 (Jan. 10, 2023), pp. 87–97. doi: 10.1021/acsomega.2c06044.

[39] Gerard Deckert et al. “The Complete Genome of the Hyperthermophilic Bacterium Aquifex Aeolicus”. In: *Nature* 392.6674 (Mar. 1998), pp. 353–358. doi: 10.1038/32831.

[40] Marianne Guiral and Marie-Thérèse Giudici-Orticoni. “Microbe Profile: Aquifex Aeolicus: An Extreme Heat-Loving Bacterium That Feeds on Gases and Inorganic Chemicals: This Article Is Part of the Microbe Profiles Collection.” In: *Microbiology* 167.1 (Jan. 1, 2021). doi: 10.1099/mic.0.001010.

[41] C.M.M. Overtoom-van Aartrijk. “Studying Protein Unfolding and Translocation by the Protease FtsH with Optical Tweezers”. Delft University of Technology, 2023. doi: 10.4233/UUID:C00BAD95-F968-4693-A278-F96CC9489503.

[42] Koreaki Ito and Yoshinori Akiyama. “CELLULAR FUNCTIONS, MECHANISM OF ACTION, AND REGULATION OF FTSH PROTEASE”. In: *Annual Review of Microbiology* 59.1 (Oct. 1, 2005), pp. 211–231. doi: 10.1146/annurev.micro.59.030804.121316.

[43] V.I. Carvalho. “Biochemical and Structural Studies of FtsH, a Membrane Anchored Degradation Machine”. Delft University of Technology, 2018. doi: 10.4233/UUID:CCFB250B-48A4-487A-B6B2-10E7392C1F1A.

[44] T. Tomoyasu et al. “Escherichia Coli FtsH Is a Membrane-Bound, ATP-dependent Protease Which Degrades the Heat-Shock Transcription Factor Sigma 32.” In: *The EMBO Journal* 14.11 (June 1995), pp. 2551–2560. doi: 10.1002/j.1460-2075.1995.tb07253.x.

[45] Alibek Kruglikov, Yulong Wei, and Xuhua Xia. “Proteins from Thermophilic *Thermus Thermophilus* Often Do Not Fold Correctly in a Mesophilic Expression System Such as *Escherichia Coli*”. In: *ACS Omega* 7.42 (Oct. 25, 2022), pp. 37797–37806. doi: 10.1021/acsomega.2c04786.

[46] John E. Cronan and Kelynne E. Reed. “[27] Biotinylation of Proteins in Vivo: A Useful Posttranslational Modification for Protein Analysis”. In: *Methods in Enzymology*. Vol. 326. Elsevier, 2000, pp. 440–458. isbn: 978-0-12-182227-9. doi: 10.1016/S0076-6879(00)26069-2.

[47] Millard G Cull and Peter J. Schatz. “Biotynilation of Protein in Vivo and in Vitro Using Small Peptide Tags”. In: *Methods in Enzymology*. Vol. 326. Elsevier, 2000, pp. 430–440. isbn: 978-0-12-182227-9.

[48] Piotr E. Marszalek et al. “Mechanical Unfolding Intermediates in Titin Modules”. In: *Nature* 402.6757 (Nov. 1999), pp. 100–103. doi: 10.1038/47083.

[49] Robert B. Best et al. “Mechanical Unfolding of a Titin Ig Domain: Structure of Transition State Revealed by Combining Atomic Force Microscopy, Protein Engineering and Molecular Dynamics Simulations”. In: *Journal of Molecular Biology* 330.4 (July 2003), pp. 867–877. doi: 10.1016/S0022-2836(03)00618-1.

[50] Philip M. Williams et al. “Hidden Complexity in the Mechanical Properties of Titin”. In: *Nature* 422.6930 (Mar. 2003), pp. 446–449. doi: 10.1038/nature01517.

[51] Meghann R. Kasal et al. “Lon Degrades Stable Substrates Slowly but with Enhanced Processivity, Redefining the Attributes of a Successful AAA+ Protease”. In: *Cell Reports* 42.9 (Sept. 2023), p. 113061. doi: 10.1016/j.celrep.2023.113061.

[52] Hema Chandra Kotamarthi, Robert T. Sauer, and Tania A. Baker. “The Non-dominant AAA+ Ring in the ClpAP Protease Functions as an Anti-stalling Motor to Accelerate Protein Unfolding and Translocation”. In: *Cell Reports* 30.8 (Feb. 2020), 2644–2654.e3. doi: 10.1016/j.celrep.2020.01.110.

[53] Hongbin Li et al. “Point Mutations Alter the Mechanical Stability of Immunoglobulin Modules”. In: ().

[54] Hu Chen et al. “Dynamics of Equilibrium Folding and Unfolding Transitions of Titin Immunoglobulin Domain under Constant Forces”. In: *Journal of the American Chemical Society* 137.10 (Mar. 18, 2015), pp. 3540–3546. doi: 10.1021/ja5119368.

[55] Kai Westphal et al. “A Trapping Approach Reveals Novel Substrates and Physiological Functions of the Essential Protease FtsH in Escherichia Coli”. In: *Journal of Biological Chemistry* 287.51 (Dec. 2012), pp. 42962–42971. doi: 10.1074/jbc.M112.388470.

[56] Irfan Prabudiansyah, Ramon Van Der Valk, and Marie-Eve Aubin-Tam. “Reconstitution and Functional Characterization of the FtsH Protease in Lipid Nanodiscs”. In: *Biochimica et Biophysica Acta (BBA) - Biomembranes* 1863.2 (Feb. 2021), p. 183526. doi: 10.1016/j.bbamem.2020.183526.

[57] Sivaraj Sivaramakrishnan et al. “Dual-Beam Optical Tweezers”. In: *Encyclopedia of Biophysics*. Ed. by Gordon C. K. Roberts. Berlin, Heidelberg: Springer Berlin Heidelberg, 2013, pp. 522–526. isbn: 978-3-642-16711-9 978-3-642-16712-6. doi: 10.1007/978-3-642-16712-6_514.

[58] Dharm Singh Yadav et al. “Optical Tweezers in Biomedical Research – Progress and Techniques”. In: *Journal of Medicine and Life* 17.11 (Nov. 2024), pp. 978–993. doi: 10.25122/jml-2024-0316.

[59] Furqan M Fazal and Steven M Block. “Optical Tweezers Study Life under Tension”. In: *Nature Photonics* 5.6 (June 2011), pp. 318–321. doi: 10.1038/nphoton.2011.100.

[60] Laura Pérez-García et al. “Optimal Calibration of Optical Tweezers with Arbitrary Integration Time and Sampling Frequencies: A General Framework [Invited]”. In: *Biomedical Optics Express* 14.12 (Dec. 1, 2023), p. 6442. doi: 10.1364/BOE.495468.

[61] Fabian Czerwinski, Andrew C. Richardson, and Lene B. Oddershede. “Quantifying Noise in Optical Tweezers by Allan Variance”. In: *Optics Express* 17.15 (July 20, 2009), p. 13255. doi: 10.1364/OE.17.013255.

[62] Lora Nugent-Glandorf and Thomas T. Perkins. “Measuring 01-Nm Motion in 1 Ms in an Optical Microscope with Differential Back-Focal-Plane Detection”. In: *Optics Letters* 29.22 (Nov. 15, 2004), p. 2611. doi: 10.1364/OL.29.002611.

[63] Y. Asahara et al. “FtsH Recognizes Proteins with Unfolded Structure and Hydrolyzes the Carboxyl Side of Hydrophobic Residues”. In: *Journal of Biochemistry* 127.5 (May 1, 2000), pp. 931–937. doi: 10.1093/oxfordjournals.jbchem.a022689.

[64] Gheorghe Chistol et al. “High Degree of Coordination and Division of Labor among Subunits in a Homomeric Ring ATPase”. In: *Cell* 151.5 (Nov. 2012), pp. 1017–1028. doi: 10.1016/j.cell.2012.10.031.

[65] Hanbin Mao et al. “Temperature Control Methods in a Laser Tweezers System”. In: *Biophysical Journal* 89.2 (Aug. 2005), pp. 1308–1316. doi: 10.1529/biophysj.104.054536.

[66] Benjamin M Stinson et al. “Subunit Asymmetry and Roles of Conformational Switching in the Hexameric AAA+ Ring of ClpX”. In: *Nature Structural & Molecular Biology* 22.5 (May 2015), pp. 411–416. doi: 10.1038/nsmb.3012.

[67] Adrian O Olivares et al. “Mechanochemical Basis of Protein Degradation by a Double-Ring AAA+ Machine”. In: *Nature Structural & Molecular Biology* 21.10 (Oct. 2014), pp. 871–875. doi: 10.1038/nsmb.2885.

[68] Marie-Eve Aubin-Tam et al. “Adhesion through Single Peptide Aptamers”. In: *The Journal of Physical Chemistry A* 115.16 (Apr. 28, 2011), pp. 3657–3664. doi: 10.1021/jp1031493.

[69] Adrian O. Olivares et al. “Effect of Directional Pulling on Mechanical Protein Degradation by ATP-dependent Proteolytic Machines”. In: *Proceedings of the National Academy of Sciences* 114.31 (Aug. 2017). doi: 10.1073/pnas.1707794114.

[70] Edward C. Eckels et al. “The Mechanical Power of Titin Folding”. In: *Cell Reports* 27.6 (May 2019), 1836–1847.e4. doi: 10.1016/j.celrep.2019.04.046.

[71] Ionel Popa et al. “Nanomechanics of HaloTag Tethers”. In: *Journal of the American Chemical Society* 135.34 (Aug. 28, 2013), pp. 12762–12771. doi: 10.1021/ja4056382.

[72] Brian C. Carter, Michael Vershinin, and Steven P. Gross. “A Comparison of Step-Detection Methods: How Well Can You Do?” In: *Biophysical Journal* 94.1 (Jan. 2008), pp. 306–319. doi: 10.1529/biophysj.107.110601.

[73] Max A. Little and Nick S. Jones. “Generalized Methods and Solvers for Noise Removal from Piecewise Constant Signals. II. New Methods”. In: *Proceedings of the Royal Society A: Mathematical, Physical and Engineering Sciences* 467.2135 (Nov. 8, 2011), pp. 3115–3140. doi: 10.1098/rspa.2010.0674.

[74] Jacob W. J. Kerssemakers et al. “Assembly Dynamics of Microtubules at Molecular Resolution”. In: *Nature* 442.7103 (Aug. 2006), pp. 709–712. doi: 10.1038/nature04928.

[75] Srikesh G. Arunajadai and Wei Cheng. “Step Detection in Single-Molecule Real Time Trajectories Embedded in Correlated Noise”. In: *PLoS ONE* 8.3 (Mar. 22, 2013). Ed. by Pratul K. Agarwal, e59279. doi: 10.1371/journal.pone.0059279.

[76] Bennett Kalafut and Koen Visscher. “An Objective, Model-Independent Method for Detection of Non-Uniform Steps in Noisy Signals”. In: *Computer Physics Communications* 179.10 (Nov. 2008), pp. 716–723. doi: 10.1016/j.cpc.2008.06.008.

[77] Maarten Slik. *AVKV Stepfitting Method*. Version 1. Netherlands, 2025. url: https://github.com/MGHSlik/AVKV-step-fitting.git.

[78] Cristina Puchades et al. *Atomic Structure of the Mitochondrial Inner Membrane AAA+ Protease YME1 Reveals the Mechanism of Substrate Processing*. Sept. 15, 2017. doi: 10.1101/189316. Pre-published.

[79] Eric Botello et al. “Temperature and Chemical Denaturant Dependence of Forced Unfolding of Titin I27”. In: *The Journal of Physical Chemistry B* 113.31 (Aug. 6, 2009), pp. 10845–10848. doi: 10.1021/jp9002356.

[80] Miao Yu et al. “Unexpected Low Mechanical Stability of Titin I27 Domain at Physiologically Relevant Temperature”. In: *The Journal of Physical Chemistry Letters* 12.33 (Aug. 26, 2021), pp. 7914–7920. doi: 10.1021/acs.jpclett.1c01309.

Acknowledgements

My journey with Optical Tweezers began well before this thesis, during a lecture given by Marie-Eve when I was still a Bachelor student. I remember wanting to conduct my BSc thesis in this group, but to my initial disappointment, there were no spots available. Looking back, I am genuinely happy it turned out that way. Waiting until my Master's allowed me to dedicate the time and attention this impressive, complex technique deserves.

Marie-Eve, thank you for opening your lab to me. I learned a great deal. I am also deeply grateful to both you and Pang-Yen for looking out for me. The start and end of this thesis were marked by some personally turbulent times; I cannot thank you enough for your flexibility, for giving me space when I needed it, and for your compassion during those periods.

To my daily supervisor, Pang-Yen: thank you for guiding me through the dual worlds of experimental physics and protein biochemistry. I really enjoyed my time working with you, not just for the science, but for our laughs, and your unique insights into the cultural differences between Taiwan and the Netherlands. I wish you the best in concluding your PhD, and trust you are just one experiment removed from wrapping it up successfully!

A special thanks goes to Roland, whose technical depth was vital to my research. Thank you for helping me understand the Optical Tweezers system and for guiding me through the messed up world that is LabVIEW VIs. I can safely say I am relieved to never have to touch those interfaces. For your sake, I hope you find a solution for a Python implementation of the AOD driver software soon, so you can join me where the grass is greener and you can happily pitch your tent.

I would also like to thank Theo van Laar for his assistance with protein purification, specifically for stepping in during the most critical sample loading moments of my life. My gratitude also extends to Koen Visscher for sharing the original code for the KV algorithm, which was instrumental in my development of the AVKV Python implementation. To the rest of the group: thank you for making the days lighter and the lunches full of laughter.

Outside of the lab, I had a vital support network. To my rowing mate, Tim: thank you for helping me clear my mind. Simply getting on the water and making the most of our season was exactly the escape I sometimes needed. To Brigit: thank you for helping me remove the grammatical errors from my thesis, and the emotional errors from my brain.

I must also acknowledge the unknown Applied Sciences Faculty worker who, by administrative accident, granted me access to the coffee machines across the university. I would probably still be writing this thesis if not for that mistake.

Finally, to my friends, family, and housemates: thank you for your support and for patiently listening to my monologues about tiny things no one can even see.

Maarten Slik
Delft, December 2025

7

Supplemental Information

7.1. Biochemical Assays

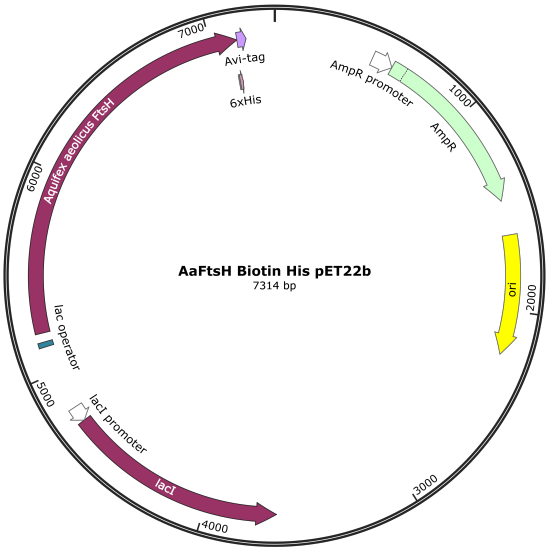

Figure 7.1: Plasmid map of pET22b for IPTG-inducible expression of AaFtsH in *E. coli*.
The construct features a lac operator (dark blue) upstream of the AaFtsH gene (purple), with C-terminal His- and Avi-tag, an ampicillin resistance cassette AmpR (green), and the lacI repressor gene (orange) for tight regulation of transcription. The replication origin (yellow) is indicated as well.

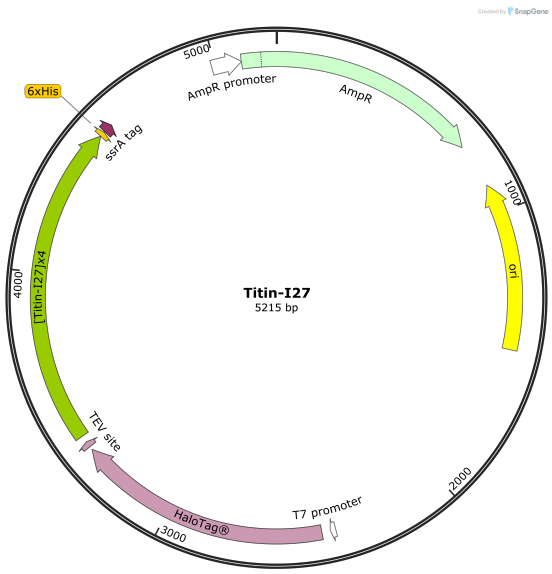

Figure 7.2: Plasmid map of pET22b for expression of the Halo-titin-[I27]x4-ssrA construct in *E. coli*.
The plasmid contains a T7 promoter (white) upstream of the substrate construct. The construct is built up by a HaloTag (pink), the titin-I27 domain repeat (green), a His-tag (orange), and a C-terminal ssrA-tag (purple). Additionally, the plasmid contains an ampicillin resistance cassette AmpR (light green). The replication origin (yellow) is indicated as well.

7.2. Setup Calibration & Validation

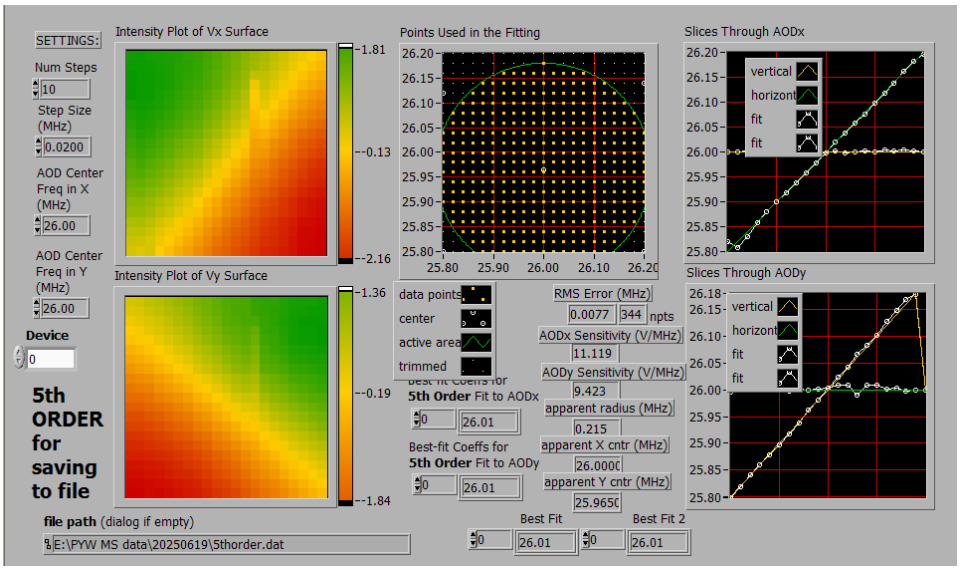

Figure 7.3: Screenshot of the Labview VI which handles position calibration of a trapped bead
The intensity profile of the V_x and V_y surface are plotted (left). The user can set a number of steps and step size to set the grid size over which the trapped bead is scanned (upper middle). A slice through x and y is plotted to indicate the measurements within the linear region (right). For this specific calibration the linear region is ~± 0.20MHz = ~± 200nm. Additionally, RMS error, AOD sensitivity and fitted centers are calculated and shown (lower middle).

7.2.1. Determination of Trap Stiffness via Corner Frequency Analysis

Modeling the Trapped Bead: Langevin Equation

A spherical bead of radius r in a fluid of viscosity η experiences a **restoring force** from the optical trap ($F_{trap} = -\kappa x$), a **drag force** due to the fluid ($F_{drag} = -\gamma \dot{x}$), and a **random thermal force** (F_{th}) with zero mean and variance. These forces are combined in the Langevin equation (Equation 7.1):

$$\gamma\dot{x}(t) + \kappa x(t) = F_{\text{th}}(t), \tag{7.1}$$

To analyze the bead's motion in the frequency domain, we take the Fourier transform of Equation 7.1:

$$\gamma(i2\pi f)\tilde{x}(f) + \kappa\tilde{x}(f) = \tilde{F}_{\text{th}}(f) \tag{7.2}$$

$$\tilde{x}(f) = \frac{\tilde{F}_{\text{th}}(f)}{\gamma(i2\pi f) + \kappa} \tag{7.3}$$

The power spectral density (PSD) of the position fluctuations is given by:

$$S_x(f) = \lim_{T\to\infty} \frac{1}{T}\langle|\tilde{x}(f)|^2\rangle, \tag{7.4}$$

Substituting Equation 7.3 into Equation 7.4, using the property that ($\langle|\tilde{F}_{\text{th}}(f)|^2\rangle = 2\gamma k_B T$), and simplifying, we obtain the lorentzian PSD of a harmonically trapped bead:

$$S_x(f) = \frac{2\gamma k_B T}{|\gamma(i2\pi f) + \kappa|^2} \tag{7.5}$$

$$= \frac{2k_B T\gamma}{(2\gamma\pi f)^2 + \kappa^2} \tag{7.6}$$

$$= \frac{2k_B T}{\gamma} \cdot \frac{1}{(2\pi f)^2 + \left(\frac{\kappa}{\gamma}\right)^2} \tag{7.7}$$

Corner Frequency and Trap Stiffness

The PSD in Equation 7.7 has a characteristic corner frequency $f_c = \frac{\kappa}{2\pi\gamma}$, the frequency at which the PSD drops to half its low-frequency value. We can rearrange Equation 7.7 with the definition for the corner frequency to yield the trap stiffness:

$$\kappa = 2\pi\gamma f_c. \tag{7.8}$$

Where the drag coefficient γ is calculated with Stokes' law: $\gamma = 6\pi\eta r$, with η as the fluid viscosity, and r as the bead radius.

Figure 7.4: Corner frequency analysis of free trapped bead.
Corner frequency is determined from the power spectral density of position signal of the bead. The trap stiffness is determined from Equation 7.8, yielding $k_x = 0.133pNnm^{-1}, k_y = 0.133pNnm^{-1}$ for bead 1, recorded on 23–11–2025.

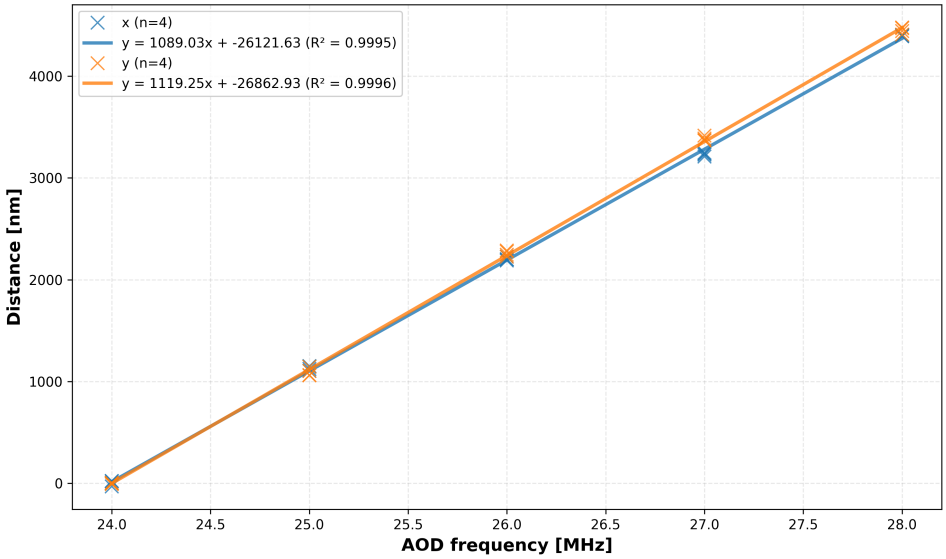

Figure 7.5: AOD frequency-to-position calibration.
Trap displacement as a function of AOD driving frequency in X (blue) and Y (orange) direction. All data (n = 4 measurements) is plotted with a linear fit to the data. Fitting yields a conversion factor $\alpha_x = 1089.03 \pm 5.6$ nm/MHz, and $\alpha_y = 1119.25 \pm 5.5$ ($R^2 > 0.999$).

7.3. AVKV validation

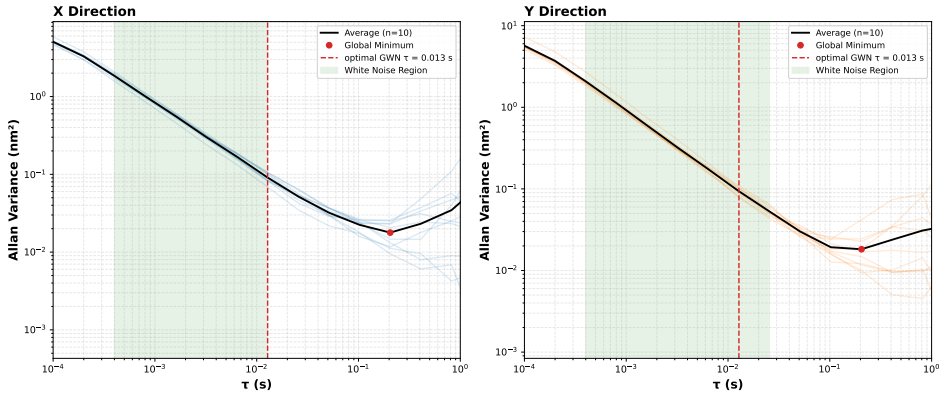

Figure 7.6: AV-based determination of optimal sampling frequency for KV step fitting.
Allan variance analysis on a measurement series (n=10) recorded on a single day. From the loglog plot, the GWN bandwidth is determined for each lateral direction. The τ offering highest positional accuracy from the union of X- and Y-GWN bandwidth is chosen as the optimal sampling frequency for KV step fitting.